# Components of near-surface energy balance derived from satellite soundings: i. Midday net available energy

Kaniska Mallick[1], Andrew Jarvis[2], Georg Wohlfahrt[3], Gerard Kiely[4], Takashi Hirano[5], Akira Miyata[6], Susumu Yamamoto[7], Lucien Hoffmann[1]

[1]Department of Environment and Agro-biotechnologies, Centre de Recherche Public, Gabriel Lippmann, L4422, Luxembourg

[2]Lancaster Environment Centre, Lancaster University, LA1 4YQ, United Kingdom

[3]Ecosystem Research & Landscape Ecology, University of Innsbruck, Innsbruck, Austria, A-6020

[4]Hydrometeorology Research Group, Department of Civil and Environmental Engineering, University College Cork, Ireland.

[5]Division of Environmental Resources, Research Faculty of Agriculture, Hokkaido University, Hokkaido, Japan

[6]National Institute for Agro-Environmental Sciences, Tsukuba, Japan

[7]Graduate School of Environmental Science, Okayama University Tsushimanaka3-1-1, Okayama 700-8530

# Corresponding author. Tel.: +352 470261425 *E-Mail:* kaniska.mallick@gmail.com (K. Mallick)

## Abstract

20     This paper introduces a relatively simple method for recovering global fields of monthly midday (13:30 hour) near-surface net available energy (the sum of the sensible and latent heat flux or the difference between the net radiation and surface heat accumulation) using satellite visible and infra-red products derived from the AIRS (Atmospheric Infrared Sounder) and MODIS (MOderate Resolution Imaging

25     Spectroradiometer) platforms. The method focuses on first specifying net surface radiation by considering its various shortwave and longwave components. This was then used in a surface energy balance equation in conjunction with satellite day-night surface temperature difference to derive 12 hour discrete time estimates of surface, system heat capacity and heat accumulation, leading directly to retrieval for surface net available

30     energy. Both net radiation and net available energy estimates were evaluated against ground truth data taken from 30 terrestrial tower sites affiliated to the FLUXNET network covering 7 different biome classes. This revealed a relatively good agreement between the satellite and tower data, with a pooled root mean square deviation of 98 and 72 W $m^{-2}$ for monthly 13:30 hour net radiation and net available energy respectively,

35     although both quantities were underestimated by approximately 25 and 10 percent respectively relative to the tower observation. Analysis of the individual shortwave and longwave components of the net radiation revealed the downwelling shortwave radiation to be main source of this systematic underestimation.

**Key words:** Net radiation, net available energy, satellite, AIRS, MODIS, eddy
40     covariance tower.

## 1 Introduction

    An important manifestation of climate change is widespread alteration of the composition of the energy balance at the Earth's surface (Trenberth et al., 2009; Wild et al., 2013). Given the importance of being able to predict the consequences of climate change, both measurement and modelling of the components of surface energy balance

45     attract significant attention from a broad range of related scientific disciplines (Stephens et al., 2012). Two such disciplines are hydrology and meteorology, which share a

common interest in resolving the balance between sensible, H, and latent, λE, heat fluxes over a broad range of spatial and temporal scales (Anderson et al., 2012).

Net available energy, $\Phi$, is a core variable used to predict the magnitude of H and λE given it is defined as the sum of these two fluxes (Wright et al., 1992, Migletta et al., 2009; Anderson et al., 2012),

$$\Phi = \lambda E + H \tag{1}$$

The utility of this definition arises from being able to also specify $\Phi$ as the difference between the net broadband radiation, $R_N$, and the rate of heat accumulation, G, below the plain across which $R_N$ is specified,

$$\Phi = R_N - G \tag{2}$$

Given $R_N$ is routinely measured using net radiometers this affords an opportunity to specify $\Phi$ and hence either H or λE. For example, in modelling studies λE is invariably specified as a function of $\Phi$ using the ubiquitous equations such as those of Penman (1948) for open water or Monteith (1965) for land surfaces (Mu et al., 2011, Mallick et al., 2014a). Despite being the rate of change of heat stock in terrestrial environments, G is often interpreted as the 'ground heat flux' and attempts to measure this using heat flux plates are commonplace (Mayocchi and Bristow, 1995; Sauer and Horton, 2005; Heitman et al., 2010). These measurements prove somewhat less reliable than $R_N$ due to greater spatial heterogeneity in ground heat uptake (Gao et al., 1998; Tittebrand and Berger, 2009; Verhoef et al., 2012) allied to the fact that significant heat capacity resides in other elements of the land surface (Ochsner et al., 2007). As a result, G proves problematic in surface energy balance studies and is either ignored (Foken et al., 2006; Foken, 2008) or treated somewhat superficially (Choudhury, 1987), despite being significant under a broad range of conditions (Santanello and Friedl, 2003; Ochsner et al., 2007). Large scale estimates of G are useful in the context of regional and global evapotranspiration modeling and for verification of regional and Global Circulation Models (Kergoat et al., 2011).

The arrival of satellite retrievals for many of the components of $R_N$ has opened up opportunities to develop large scale estimates of this variable and hence $\lambda E$ (Batra et al., 2006; Mu et al., 2007, Anderson et al., 2012). For example, retrievals for the components of $R_N$ have been available through the International Satellite Cloud Climatology Project (ISCCP) (Pinker and Laszlo, 1992; Stephens et al., 2012); the Earth Radiation Budget Experiment (ERBE) (Priestley et al., 2011); Clouds and Earth's Radiant Energy System (CERES) (Mlynczak et al., 2011, Chen et al., 2013) on board of the NASA Earth Observing System (EOS) and Tropical Rainfall Measuring Mission (TRMM) satellites (Wielicki et al., 1998). Several studies have reported the estimation of $R_N$ using a combination of MODIS (MOderate Resolution Imaging Spectroradiometer) atmospheric and land products over USA, China, and India (Cai et al., 2007; Mallick et al., 2009; Bisht and Bras, 2010, 2011) or NOAA-14 (National Oceanic and Atmospheric Administration) data over the Tibetan Plateau (Ma et al., 2002).

Unfortunately, in the absence of direct observations of G at spatial scales and coverage of satellite $R_N$, retrievals for $\Phi$ have had to rely on the parameterisation of G using surface temperature, albedo and vegetation index information (Bastiaanssen et al., 1998; Batra et al., 2006) or by assigning some fixed proportion of $R_N$ (Choudhury, 1987; Humes et al., 1994) in satellite-based surface energy balance models (Mecikalski et al., 1999; Anderson et al., 2012). But studies by Murray and Verhoef (2007), Hsieh et al. (2009) and recently Verhoef et al. (2012) also demonstrated that G is, by definition, a highly dynamic quantity, and that the ratio $G/R_N$ can range anywhere from 0.05 to 0.50 depending on the time of day, soil moisture and thermal properties, and vegetation density. Therefore, methods that are able to provide defensible estimates of G in conjunction with $R_N$ would clearly be of great benefit to this area for determining $\Phi$ directly from satellite data and without relying unduly on any offline calibration. In this paper we present a method for retrieving $R_N$ and $\Phi$ based on exploring both satellite radiance data and day-night surface temperature difference. The approach is necessarily simple in order to avoid over reliance on models in the pre-processing and to reflect the fact that the focus of this work is the production of satellite estimates of monthly midday (13:30 hour) $\Phi$ for use in a simple Bowen ratio (Bowen, 1926) $\lambda E$ specification

framework as detailed in a companion paper by Mallick et al. (2014b) (we referrer this as M2 hereafter). Taking advantage of the extensive network of terrestrial eddy covariance tower sites (Baldocchi et al., 2001) which record direct measurements of $R_N$, H and $\lambda$E, we use these measurements to derive independent non-radiative estimates of $\Phi$ in order to critically evaluate our satellite estimates of this quantity.

The method we present here for estimating $R_N$ contrasts with more sophisticated model-based approaches which attempt to accommodate the complexity of atmospheric radiative transfer explicitly (e.g. Fouquart and Bonnel, 1980; Mlawer et al., 1997; Bisht and Bras, 2010, 2011; Hou et al., 2014). There are several reasons for adopting this stance. Firstly, the estimates of $R_N$ need to be sympathetic with the simple dynamic energy balance used to accommodate G when specifying $\Phi$. Secondly, we believe it to be important that the complexity of the methods used here are commensurate with those used in the simple Bowen ratio approach as described in M2. Related to this, we have tried to restrict the approach to largely using only AIRS data which provides the satellite soundings required for the Bowen ratio estimates. This single platform approach is to ensure the estimates do not suffer unduly from blending different data sources. Finally, as with this method, complex radiative transfer approaches are also prone to the effects of uncertainty (Betts et al., 1993; Morcrette, 2002; Seidel et al., 2010) and, therefore, the parsimony implicit in the methods used here may be seen as advantageous.

## 2 Methodology

### 2.1 Satellite datasets

In the present study two different data sources were used for the estimation of $R_N$ and $\Phi$, AIRS (Atmospheric InfraRed Sounder) and MODIS (Moderate Resolution Imaging Spectroradiometer). The AIRS sounder is carried by the NASA Aqua satellite, which was launched into a sun-synchronous low Earth orbit on May 4, 2002 as part of the NASA Earth Observing System. It gives near global coverage twice daily at 1:30 am-pm from an altitude of 705 km. Level 3 standard monthly day-night data products of air temperature and relative humidity profiles, cloud cover fraction, surface emissivity, near-surface air temperature and surface-skin temperature and columnar total precipitable water at 1° x 1°

130   spatial resolution were obtained for 2003 from the online data archive of AIRS, distributed through NASA Mirador data holdings (http://mirador.gsfc.nasa.gov/). The monthly products are simply the arithmetic mean, weighted by counts, of the daily data of each grid box. The multi-day merged products have been used here because the IR retrievals are not cloud proof and the multi-day product gave decent spatial cover in light

135   of the missing cloudy sky data. The data products were obtained in hierarchical data format (HDF4) along with their latitude-longitude projection. It is also important to mention that the daily 1 degree data contains orbital gaps and cloud contamination. In the 8-day data the co-incident land surface temperature in both day and night pass was missing and the atmospheric soundings were also missing in many places. It is the

140   monthly dataset where the soundings as well as both the day-night land surface temperatures were available and the data has complete global coverage.

We have used the MODIS Aqua atmospheric product datasets (MYD08_D3) (http://modis-atmos.gsfc.nasa.gov/index.html) at 1° x 1° spatial resolution for extracting the solar zenith angle field. For generating the surface albedo fields we used narrowband

145   surface reflectances from combined MODIS Terra-Aqua 16 day data (MCD43C4) products acquired from the MODIS data archive (http://ladsweb.nascom.nasa.gov/data/search.html). The native spatial resolution of the MCD43C4 datasets is 0.05 degree. Therefore, all the narrowband surface reflectances were first resized into 1° by 1° to make them compatible with the AIRS spatial resolution

150   and then the broadband surface albedo was generated from the narrowband reflectances following Liang et al. (1999) (presented in next section). It is important to mention that MODIS global albedo product (MCD43C3) contains bi-hemispherical reflectance (white-sky albedo) and directional hemispherical reflectance (black-sky albedo). Blue sky albedo can be determined by weighting the white and black-sky albedo with diffuse skylight

155   fraction which is a function of the aerosol optical depth and solar zenith angle. Look/up table based aerosol information and parameters are needed to convert the reflectances into the blue-sky albedo. But there are established formulations (Liang et al., 1999, Liang, 2002) to directly convert the narrowband reflectances into the broadband visible

6

albedo that does not depend on any atmospheric variables and look-up tables and
160    therefore narrowband surface reflectances are used in the present study.

One of the core objectives of the work is to explore the potential of atmospheric
sounding data. AIRS is the only dedicated sounder available which can be explored to
address the objectives in the paper. Although MODIS has soundings, but it was not
designed for this and only has low quality air temperature soundings. Coarse spatial
165    resolution of AIRS would introduces many difficulties when it comes to the evaluation,
but the most important aspect of the two companion papers (we refer the current one as
M1) is to introduce the possibility of using atmospheric sounding data as a means of
observing surface energy fluxes (a companion paper on latent and sensible heat flux,
M2). We have restricted $\Phi$ derivation to (largely) AIRS data (we use MODIS albedo
170    because AIRS does not contain any albedo field) in order to exploit a single platform for
the entire framework. We would also emphasize that the $\Phi$ retrievals are on one time slot
per day for 13:30 local time, which is a standard for the studies that use polar orbiting
satellites.

## 2.2 Net radiation

175    The approach for estimating $R_N$ uses the Atmospheric Infrared Sounder (AIRS)
radiation products, although we have also made use of the MODIS surface reflectance
and solar zenith angle products where necessary. $R_N$ is generated by considering the
following balance between net shortwave ($R_{NS}$) and longwave ($R_{NL}$) radiation at or near
the Earth's surface,

180    $$R_N = R_{NS} + R_{NL} = (1-\alpha)R_{S\downarrow} + R_{L\downarrow} - R_{L\uparrow} \qquad (3)$$

where $\alpha$ is the surface albedo and $R_{L\downarrow}$ and $R_{L\uparrow}$ are the downwelling and upwelling thermal
radiative fluxes and $R_{S\downarrow}$ is the downwelling shortwave radiative flux (all fluxes specified
in W m$^{-2}$). Our chosen reference level for $R_N$ is the near surface given this corresponds to
the flux-based tower estimates we used in the evaluation. Therefore, surface $R_{S\downarrow}$ was
185    estimated from its top-of-atmosphere clear sky counterpart $R_{S0\downarrow}$ and AIRS cloud cover
fraction (f) following Hildebrandt et al. (2007),

$$R_{S\downarrow} = (1-f)\tau_A R_{S0\downarrow} \tag{4}$$

where $\tau_A$ is the clear sky transmissivity of the atmosphere which we assume is 0.75 (Cano et al., 1986; Thornton and Running, 1999; Hildebrandt et al., 2007, Gubler et al., 2012). Although clearly a simplification, a constant clear sky transmissivity is widely used (e.g. Massaquoi, 1988; Bindi et al., 1992; Choudhury, 2001; Hildebrandt et al., 2007; Mallick et al., 2009) in recognition of the absence of robust alternatives. In addition, exploiting the AIRS cloud cover fraction data in equation (4) should help accommodate the effects of variations in both the aerosol optical depth (Kaufman and Koran, 2006; Quass et al., 2010) and atmospheric water vapor (Adhikari et al., 2006).

The terrestrial surface albedo was generated using the MODIS Aqua-Terra surface reflectances $r_i$ following Liang et al. (1999),

$$\alpha = \sum_{i=1}^{N} p_i r_i + 0.0036 \tag{5}$$

where $r_i$ are the mid-point reflectances within the $0.62 - 0.67$; $0.841 - 0.876$; $0.459 - 0.479$; $1.230 - 1.250$; $1.628 - 1.653$; $1.628 - 1.653$; and $2.105 - 2.155$ µm wavelength bands and $p_i$ are the weightings for each wavelength bands taken as $p_i$ = [0.3973; 0.2382; 0.3489; -0.2655; 0.1604; -0.0138; 0.0682] (Liang et al., 1999; 2002). The albedo of the ocean varies according to the cosine of solar zenith angle (Jin et al., 2004). Given the oceanic surface reflectances are not available in either MODIS or AIRS, a constant albedo of 0.04 was assumed for oceans given the satellite radiances are nadir.

Many of the longwave components of the radiative balance are very closely related to the raw IR radiances being measured by AIRS. Given these are not in the public domain we have attempted to recover them as follows, although in future we would anticipate using the raw IR radiances more directly if possible. $R_{NL}$ was calculated as,

$$R_{NL} = R_{L\downarrow} - R_{L\uparrow} = \varepsilon_C \varepsilon_S \sigma T_C^4 - \varepsilon_S \sigma T_S^4 \tag{6}$$

where $\sigma$ is the Stefan-Boltzmann constant ($5.67 \times 10^{-8}$ W m$^{-2}$ K$^{-4}$), $T_c$ is the columnar air temperature, and $\varepsilon_C$ and $\varepsilon_S$ are the column and surface emissivities. Among the different

8

schemes for calculating $\varepsilon_C$ we have used the formulation proposed by Prata (1996) given this appears to be the most reliable (Niemela et al., 2001; Bisht and Bras, 2010, 2011). This scheme uses AIRS total precipitable water ($\xi$) (cm) information to estimate $\varepsilon_C$ as,

$$\varepsilon_C = 1 - (1 + \xi)e^{-(1.2+3\xi)^{0.5}} \tag{7}$$

The columnar air temperature $T_C$ in equation (6) is taken as the average of the 2 m and 1000 hPa pressure level AIRS temperatures in an attempt to reflect a weighting toward the lower troposphere when specifying $R_{L\downarrow}$. $T_S$ and $\varepsilon_S$ are taken directly from the AIRS skin temperature and surface emissivity products.

## 2.3 Surface heat capacity, ground heat flux and net available energy

The definition of G stems from consideration of the non-steady state surface energy balance,

$$c\frac{dT_S(t)}{dt} = R_N(t) - \lambda E(t) - H(t) = G(t) \tag{8}$$

where $c$ is the aggregate surface system heat capacity (MJ m$^{-2}$ K$^{-1}$). The AIRS sounder platform samples twice daily at 01:30 and 13:30 hours. Despite being somewhat coarse, taking a discrete time, backward difference approximation of equation (8) with a sample interval of $\Delta t = 12$ hours equivalent to that of the AIRS pass gives,

$$\Delta T_S(t) = b_1 R_N(t) + b_2 \tag{9}$$

where $\Delta T_s$ is the day − night surface temperature change, $b_1 = \Delta t/c$ and $b_2 = -\Phi(t)\Delta t/c$. If we assume that the system is approximately in equilibrium over a 24 hour cycle, and that at 01:30 hours $\Phi \approx 0$ (for all 30 sites analysed in this study $\Phi(01:30) < 0.05\Phi(13:30)$; see also Tamai et al., 1998; Mamadou et al., 2014), then this gives the following simultaneous equations:

$$\Delta T_S(13:30) = b_1 R_N(13:30) + b_2 \tag{10a}$$

$$-\Delta T_S(13:30) = b_1 R_N(1:30) \tag{10b}$$

9

230   which can be solved analytically to derive $b_1$ and $b_2$ and hence $\Phi$ and c for each grid cell in the AIRS global array.

Equation (10) is a coarse approximation of equation (8) and hence potentially suffers from a number of deficiencies. Firstly, diurnal symmetry in $\Delta T_s$ is only appropriate when one considers weekly or monthly average behaviour, and that there are no additional heat

235   losses or gains to/from stores beyond the domain defined by the single heat capacity c. In this study we examined the monthly average behaviour because AIRS only gives partial global coverage on the daily timescale due to both cloud effects and the non-overlapping swath width of the sensor. Interactions with additional long term heat stores is an issue in systems such as the oceans where there can be a persistent heat loss/gains to/from deeper

240   water over timescales of weeks to months, although relative to the diurnal fluctuation of stored surface heat this tends to be small (Stramma et al., 1986). Secondly, $\Phi$ can be either positive or negative at 01:30, although it tends to be only a fraction (never exceed 5% of afternoon $\Phi$) of its 13:30 value due to the supply of relatively small energy at night compared to the day. This may be less true for areas of land in the height of winter with

245   cloud full days and over the sea where significant daytime heat accumulation could in part be re-released as night time latent and sensible heat. Thirdly, equations 9 and 10 attribute the magnitude of the daytime G to the nighttime net long wave radiative balance, which is obviously rather uncertain. Fourthly, the air emissivity computation using Prata's equation was developed for the daytime and using it for the nighttime emissivity

250   may introduce errors. Finally, all the terms in equation (8) are highly dynamic and yet are treated as constant or varying linearly over the 12 hour sample interval. It is difficult to predict what the consequences of this are, given it depends on the pattern of radiative forcing through the day which can vary significantly in both time and space. Some illustrative examples of the theoretical assumptions of equation 10 (a and b) are depicted

255   in Figures 2, 3 and 4. Figure 2 shows the examples of the diurnal symmetry of $T_S$ for clear days in three different seasons where the saw-tooth pattern between noon (13:30 hour) and night (1:30 hour) $T_S$ is evident. This clearly shows how well these two $T_S$ samples capture the dynamic range of the day and hence the discretisation is representative of the daily energy balance. Figure 3 (a to d) illustrates the diurnal

evolution of $\Phi$ during three different times of the year (spring, summer, and winter) for four broad biome categories (grassland, cropland, forest and savanna), which clearly indicates $\Phi \cong 0$ at 1:30 hours local time and within less than 5% of afternoon $\Phi$. Lastly, Figure 4 highlighted the two dimensional relationship between the noontime G (13:30 hours) and nighttime $R_{NL}$ (1:30 hours) for the above mentioned four biomes and the correlation between the two varied between 0.32 to 0.60, having high correlation over grassland and savanna and moderate correlation over forest and cropland. Despite large differences in the footprint size between G and $R_{NL}$ measurements, the inverse relationship between the two variables in Figure 4 clearly indicates the dependence of noontime G on the nighttime longwave radiation balance. Therefore, although the theoretical approximations in equation 8 and 10 (a, b) seems to be somewhat coarse and might be deficient in some aspects (as described above), but from the Figures (2, 3, and 4) there appears to a strong connection between $\Delta T_S$, nighttime $R_N$ (or nighttime $R_{NL}$) and noontime $\Phi$. However, given the structure of the atmosphere and the very small energy fluxes involved, high latitude $\Phi$ estimates from this method are likely to be problematic anyhow.

### 2.4 Sensitivity analysis

A general sensitivity analysis was carried out in order to assess the effects of the propagation of uncertainty onto the estimates of G, $R_N$ and $\Phi$. For this analysis the input terms were assigned uniform prior distributions of $\pm$ 10 % for all parameters other than temperatures for which $\pm$ 1 K uniform prior distributions were assumed. These assumed ranges resemble the stated uncertainties as given in the AIRS support literature (Aumann et al., 2003; Hearty et al., 2014). The sensitivity of each output to each input was calculated assuming an average, locally linear sensitivity. These were expressed as the change in output per unit change in input, normalised by the median value of each. Only absolute sensitivities > 0.1 were considered significant. The standard deviation of the estimated distributions of G, $R_N$ and $\Phi$ were used as the summary statistic for the measurement uncertainty of the proposed methodology.

11

**2.5 Evaluation of $R_N$ and $\Phi$**

To evaluate the satellite values of $R_N$ and $\Phi$ we have made use of the extensive FLUXNET terrestrial tower network (Baldocchi et al., 2001). Clearly, there is a scale conflict here with the satellite retrievals being 1° whilst the individual tower observations are for scales of the order of 1 km or less. The tower $R_N$ are from the broadband net radiometer sensors located on each tower. In the absence of reliable measures of G at the tower scale and in order to derive genuinely independent measures of $\Phi$ against which to evaluate the satellite data, we have taken the tower net available energy as the sum of the measured sensible and latent heat flux i.e. equation (1). Thereby we have assumed that the eddy covariance flux measurements are able to close the energy balance (i.e. $R_N$ - G = $\lambda E$ + H), the implications of which will be discussed below. We have chosen 30 sites covering a broad range of geographical locations selected from 7 land cover types including; evergreen broadleaf forest (EBF), mixed forest (MF), evergreen needle forest (ENF), deciduous broadleaf forest (DBF), savanna (SAV), grassland (GRA) and cropland (CRO). A comprehensive list of the site characteristics are provided in Table 1. Each tower evaluation dataset is comprised of the 13:30 hour local time samples of $R_N$, H and $\lambda E$ which correspond with the satellite overpass. Again, the evaluation is based on pooling these data into weighted monthly average values. For the evaluation we have elected to compare all 12 months of data for 2003 given this had the best overlap between the FLUXNET and AIRS databases. However before directly validating the satellite retrieved $\Phi$, the proposed $\Phi$ retrieval method is first evaluated using high temporal frequency ground based observations of $R_N$ and $T_S$ over some eddy covariance sites representing four broad biome categories (grassland, cropland, forest and savanna). Both $R_N$ and $T_S$ at 13:30 and 1:30 hours local times were extracted from half-hourly measurements and $\Phi$ at 13:30 hours was determined using equation 10 (a and b). The retrieved midday $\Phi$ was validated against tower observed latent and sensible heat fluxes.

## 3 Results

Table 2 shows the results from the sensitivity analysis. For G we see the importance of the long wave specification and in particular $\varepsilon_C$. The standard deviation of the estimate of G from the ensemble is 18 W m$^{-2}$ giving approximate 95 percent confidence detection

limits of $\pm 36$ W m$^{-2}$ on the estimates. $R_N$ is sensitive to all components of the radiation balance calculation as expected (Table 2). The standard deviation of the estimate of $R_N$ from the ensemble is 40 W m$^{-2}$ giving approximate 95 percent detection limits of $\pm 80$ W m$^{-2}$ on the estimates (Table 2). Not surprisingly the sensitivity results for $\Phi$ mirror those of $R_N$ albeit with a marginally higher ensemble standard deviation of 44 W m$^{-2}$ (Table 2).

The locations of the 30 terrestrial evaluation sites are marked in Figure 1. Figure 5 shows annual average, global satellite scenes for 13:30 hour $R_N$, c, G and $\Phi$ for the year 2003. Missing data in the images are mainly due to missing data in the AIRS soundings at high latitudes or over the mountain belts where it is difficult to profile air temperature and relative humidity reliably. In addition, persistent cloudy conditions also prevent reliable retrieval and hence are rejected although these will be less evident in the monthly or annual average data.

Figure 5a shows the global distribution of $R_N$ which generally decreases with latitude as expected. $R_N$ also decreases over land due to the generally higher albedo resulting in reduced absorption of the net shortwave radiation (Giambelluca et al., 1997, Gao and Wu, 2014) or relatively higher surface temperature increasing the net longwave component, especially over the drier regions (Liang et al., 1998, Trenberth, 2011). As a result the magnitude of $R_N$ was around 200 – 300 W m$^{-2}$ over the dry desert regions whereas the oceanic values of $R_N$ were 450 – 700 W m$^{-2}$.

Figure 5b shows the global distribution of c (surface heat capacity). The oceanic values of 4 to 8 MJ m$^{-2}$ K$^{-1}$ are equivalent to 1 to 2 m of sea water, which appears reasonable on the daily time step to which they relate (Stramma et al. 1986; Schwartz, 2007). These oceanic values are somewhat noisy due to the small day-night temperature differences observed for the oceans giving a relatively poor signal to noise ratio. However, behind this noise the pattern of oceanic c appears relatively uniform as one might expect. Over land c varies between 0.05 – 0.5 MJ m$^{-2}$ K$^{-1}$ with wetter tropical and high latitude areas showing significantly higher values than the drier, less vegetated areas as expected. The soil equivalent depth of this heat capacity is approximately 0.01 m,

13

which again appears reasonable for a daily time step (Li and Islam, 1999), although in heavily vegetated areas c is obviously comprised of a more complex aggregation.

Figure 5c shows the global distribution of G. These are the 13:30 hour values, hence being net positive as an annual average. Between 20º North-South G is approximately 10 to 20 percent of $R_N$, and this rises to more than 40 percent above 50º North-South (Hsieh et al., 2009). Given this opposes the pattern of $R_N$ one would conclude either some deficiencies in the way G is specified here or that $R_N$ partitions into latent heat far more effectively than surface heating in these warm wet environments (Liu et al., 2005). Again, terrestrial values are lower than their oceanic equivalents mainly due to the lower heat capacity as well as reduced $R_N$ as discussed above. This also highlights the role of the vegetation layer in preventing ground heating (Baker and Baker, 2002; Bounoua et al., 2010). The Sahara appears particularly prominent in this scene with high rates of midday heat accumulation which appears to be associated with a combination of moderate net radiation and relatively high heat capacity. The heterogeneity in this region appears to be related to the pattern of bare darker rock.

Figure 5d shows the global distribution of $\Phi$ which follows a similar pattern to $R_N$ as expected, although the pattern of G shown in Figure 5c dictates that the North-South gradients in $\Phi$ are somewhat stronger than those of $R_N$. Before discussing these results we consider their evaluation. In the first step, we validated the new method of $\Phi$ retrieval at representative FLUXNET sites using ground observations of the surface radiation components ($T_S$, $R_N$ and G) as input before directly evaluating the satellite based retrievals. Tower scale evaluation of daily midday (13:30 hours) $\Phi$ is illustrated in Figure 6 (a, b, c, and d) for four broad biome categories, which shows a modest correlation [r = 0.91($\pm$0.03)[1] to 0.98 ($\pm$0.04)] between observed and predicted $\Phi$ across all the biomes with regression statistics ranging between 0.89 ($\pm$0.07) to 1.12 ($\pm$0.05) for the gain and -44.29 ($\pm$20.15) to 59.40 ($\pm$29.03) for the offset, respectively (Figure 6). The root mean square deviation (RMSD) varied between 41 (savanna) to 88 W m$^{-2}$ (forest).

---

[1] All uncertainties are expressed as $\pm$ one standard deviation unless otherwise stated.

Figure 7a shows the pooled evaluation of satellite $R_N$ which produced an overall correlation of r = 0.88 (±0.03). Assuming both tower and satellite observations are linearly related through some 'true' value, then the pooled values are co-related by $R_N$(satellite) = 0.75(±0.02)$R_N$(tower)+23.37(±8.20) i.e. a small but significant underestimation in $R_N$(satellite) relative to $R_N$(tower). The root mean square deviation (RMSD) between the two was 98 W m$^{-2}$. The biome specific statistics for $R_N$ are given in Table 3 which reveals correlations ranging between 0.65 (EBF) to 0.96 (ENF), RMSD ranging between 74 (GRA) to 127 W m$^{-2}$ (EBF) and regression statistics ranging between 0.58 (±0.08) to 0.87 (±0.04) for the gain and -32.40 (±23.73) to 107.45 (±39.93) for the offset.

Figure 7b shows the evaluation for $\Phi$ which produced pooled statistics of r = 0.87 (±0.03), RMSD of 72 W m$^{-2}$ and the regression between the satellite predicted and tower observed $\Phi$ produced a regression line of $\Phi$(satellite) = 0.90(±0.03)$\Phi$(tower)–2.43 (±8.19). The biome specific statistics for $\Phi$ are also given in Table 3 showing correlations ranging from 0.70 (EBF) to 0.95 (ENF), RMSD ranging between 62 (GRA & SAV) to 88 (EBF) W m$^{-2}$ and regression coefficients ranging between 0.66 (±0.08) to 1.01 (±0.05) and -65.25 (±27.07) to 108.71 (±32.10) for the gain and offset, respectively.

Figure 8 shows a sample of monthly time series for $\Phi$ for both the satellite and the towers. The sites were selected to represent the biome classes considered here and also ones for which complete annual data sets for 2003 were available. These results show the satellite estimates generally track the trends in the tower data and hence the pooled statistics are not masking the within site variability. Again, the site-wise comparative statistics for these data are given in Table 3.

## 4 Discussion

For $R_N$ the statistics relating the satellite and tower data are different with the results of: Bisht et al. (2005) who obtained 74 W m$^{-2}$ RMSD when evaluating MODIS Terra geophysical land products over the Southern Great Plains of the US (our RMSD in grassland is only comparable here while other biomes show larger error); Jacobs et al. (2004) who obtained a 14 – 46 W m$^{-2}$ RMSD (12.2 percent relative RMSD) when

400    determining hourly $R_N$ using GOES (Geostationary Operational Environmental Satellite)
data over wetlands in the Southern Florida; Cai et al. (2007) who obtained 13.7 percent
error when evaluating MODIS Terra-Aqua data over China; Bisht and Bras (2010) who
obtained $39 - 51$ W m$^{-2}$ RMSD over the central US using MODIS terra atmospheric data
at 5-10 km spatial resolution; Hwang et al. (2013) and Hou et al. (2014) who reported

405    RMSD in instantaneous and daily $R_N$ to be $58 - 142$ W m$^{-2}$ and $37 - 40$ W m$^{-2}$ over South
east Asia and China, respectively, using MODIS terra data products. Stackhouse et al.
(2000) evaluated the International Satellite Cloud Climatology Project (ISCCP) data to
have errors in the range 10 to 15 W m$^{-2}$ in monthly average shortwave and longwave
radiative fluxes. Apart from these studies, other studies reported $33 - 60$ W m$^{-2}$ RMSD in

410    daily $R_N$ using 5 km MODIS Terra optical and thermal data (a comprehensive list of
relevant studies is given in Table 4). It is important to emphasize that, in the present study
the RMSD is being impacted in two ways; due to spatial scale mismatch and due to the
time integration. When these errors are compounded in the derivation of $R_N$ and
compared with tower data, an RMSD of the order of 98 W m$^{-2}$ appears reasonable

415    considering the coarse spatial resolution of the AIRS data (1° x 1°).

There have been very few attempts to retrieve satellite estimates of $\Phi$ and compare
these with ground truth data, although the statistics from our attempt appear to be parallel
to the results of Stisen et al. (2008) who studied a single grassland site in the Senegal
River basin using moderate (high) spatio-temporal resolution (5 km spatial resolution, 15

420    minutes temporal resolution) MSG (Meteosat Second Generation) geostationary satellite
data and obtained a correlation of r = 0.71 and an RMSD of 43 W m$^{-2}$ in comparison to
the    surface    measurements.    While    estimating    evapotranspiration    over    Indian
agroecosystems, Bhattacharya et al. (2010) obtained an RMSD of 56 W m$^{-2}$ for noontime
$\Phi$ using 8 km resolution Indian geostationary satellite data. In another study with MODIS

425    Aqua data over semi-arid agroecosystems in India, Bhattacharya et al. (2011) reported an
RMSD of 34 W m$^{-2}$ in daily average $\Phi$, which was associated with a significant tendency
to underestimate $\Phi$. Common to all these studies, the ground heat flux was either
modelled as an empirical approximation employing remotely sensed surface variables
(albedo, vegetation index and $T_S$) or as a fixed fraction of $R_N$. Murray and Verhoef

16

430    (2007) argued that these empirical approaches do not generalise well. In particular, prescribing G as a fixed fraction of $R_N$ overlooks the role played by the thermal inertia of the land surface (Santanello and Friedl, 2003) leading to an underestimation in G in the morning and overestimation during the afternoon (Gentine et al., 2007). The retrieval of G proposed here using day-night surface temperature information attempts to account for

435    this thermal inertia effect and the results appear to support this approach especially when considering the scale mismatch between the tower and satellite observations.

As seen in Figure 7a there is a systematic underestimation of $R_N$ relative to the tower values which exceeds the typical accuracy of net radiometer measurements of 20 W m$^{-2}$ quoted by Foken (2008). We examined this underestimation in more detail wherever

440    possible, by evaluating three of the individual radiation components of $R_N$ ($R_{S\downarrow}$, $R_{L\downarrow}$ and $R_{L\uparrow}$). All tower sites provided measurements of $R_{S\downarrow}$ (but not $R_{S\uparrow}$). Figure 9a shows $R_{S\downarrow}$ is systematically underestimated at the satellite scale with $R_{S\downarrow}$(satellite) = 0.70($\pm$0.02)$R_{S\downarrow}$(tower)+68($\pm$12.24) which accounts for the mismatch of $R_N$(satellite) $\approx$ 0.75$R_N$(tower). Before attempting to account for the various reasons for this

445    underestimation it is important to realise that, unlike the IR components, the shortwave components are all-sky retrievals i.e. like the tower data they do not omit cloudy sky conditions. As a result, any bias in the shortwave is not as a result of biased sampling when comprising the monthly average. Besides, the omission of non-clear sky data would tend to lead to $R_{S\downarrow}$(satellite) $> R_{S\downarrow}$(tower).

450    Clearly, the retrieval of atmospheric shortwave transmissivity ($\tau_A$) using cloud cover fraction is the principal reason for $R_{S\downarrow}$(satellite) $< R_{S\downarrow}$(tower) (Figure 9a). The sensitivity analysis presented in Table 2 is also indicating the significant sensitivity of $R_N$ and $\Phi$ to the cloud cover fraction and atmospheric transmissivity. This shows the method presented in the manuscript to estimate $R_{S\downarrow}$_needs further improvements. If we assume $\tau_A$

455    to be the principal reason for $R_{S\downarrow}$(satellite) $< R_{S\downarrow}$(tower) then a global value of 0.75 would be, on average, too low (Gueymard, 2003). A recent study of Longman et al. (2012) for the Mauna Loa Observatory (MLO) demonstrated the clear sky $\tau_A$ could go upto 0.90. Given the relatively well defined relationship between $R_{S\downarrow}$(satellite) and $R_{S\downarrow}$(tower) seen in Figure 3c one would imagine that a more sophisticated dynamic representation of $\tau_A$

17

460     would offer substantial improvements in $R_{S\downarrow}$(satellite). Retrieval of $\tau_A$ including other atmospheric (e.g., cloud optical depth, aerosol optical depth, total precipitable water etc.) and surface (for example, single scattering albedo) variables in addition to the cloud cover fraction would offer a potential possibility of refining the $R_{S\downarrow}$ estimates (Chen et al., 2014; Longman et al., 2012; Kim and Hogue, 2008). The exo-atmospheric shortwave

465     radiation frequently interacts with the clouds, aerosols and water vapor during the transmission towards the Earth's surface. This interaction is wavelength-dependent over the entire shortwave spectrum (Chen et al., 2014; Kim and Hogue, 2008; Gueymard, 2003) and therefore spectrally resolved $\tau_A$ scheme will be valuable to accurately determine $R_{S\downarrow}$. Recalibration of $\tau_A$ using the tower data is also a possibility although we

470     have avoided this given the AIRS cloud cover fraction and scale mismatch between the satellite and tower could also be implicated in the observed bias. For example, the diffuse fraction of $R_{S\downarrow}$(tower) can become enriched by surface reflected solar radiation, particularly in undulating terrain (Dubayah and Loechel, 1997; Sultan et al., 2014). Nonlinear scaling effects of surface albedo (Oliphant et al., 2003; Salomon et al, 2006)

475     can also be implicated in this because surface albedo interacts nonlinearly with surface characteristics such as surface wetness and land surface temperature (Ryu et al., 2008) or the leaf area index (Hammerle et al., 2008). Although, the RMSD of instantaneous $R_{S\downarrow}$ obtained in the present study (110 W m$^{-2}$) is different to the other studies where $R_{S\downarrow}$ retrieval was based on either using parametric (radiative transfer) models or through

480     look-up tables derived from high spatial resolution MODIS data, it is worth comparing it with the statistics of some of those studies. Table 4 summarizes the characteristics and associated errors of some of the recent $R_{S\downarrow}$ estimation studies, which shows RMSD of 36-89 W m$^{-2}$ at flux tower footprint, 54 – 137 W m$^{-2}$ at 5 km spatial resolution and 77 – 158 W m$^{-2}$ at 1° spatial resolution for the instantaneous $R_{S\downarrow}$ estimates and 20 – 39 W m$^{-2}$ for

485     the daily $R_{S\downarrow}$ (and net shortwave, $R_{NS}$) estimates. Considering the simplicity of the current approach and the large spatial scale of the AIRS data, RMSD to the order of 110 W m$^{-2}$ appears reasonable.

    To probe the specification of $R_N$ further we investigated the individual longwave radiation components in relations to measures of theses fluxes available for a limited

subset (14) of tower sites where the longwave radiative flux components were directly measured by pyrgeometers. From Figure 9b and 9c it appears that there is quite good agreement between the satellite and tower data for both $R_{L\downarrow}$ and $R_{L\uparrow}$ and that any mismatch is insufficient to explain the discrepancy in $R_N$. This is somewhat surprising for two reasons. Firstly, unlike the shortwave component, $R_L$(tower) is all sky whilst $R_L$(satellite) is only from clear sky conditions where IR retrieval is possible. As a result, one would anticipate very significant differences in the monthly average values of the longwave components. However, it is difficult to predict the effect of this biased sampling on $R_{NL}$(satellite) given that cloud interacts with both $R_{L\downarrow}$ and $R_{L\uparrow}$ in complex ways. Secondly, one would anticipate significant scaling effects from the $T^4$ nonlinearity in equation (6) which can result in a disproportionate contribution of warmer elements within the system to both $R_{L\downarrow}$ and $R_{L\uparrow}$ (Kustas and Norman, 2000; Lakshmi and Zehrfuhs, 2002, Corbari et al., 2010). The fact that these affects are not seen to any significant degree could point to compensating errors in the analysis but does not distract from the central message of the importance of the bias in the shortwave when accounting for $R_N$(satellite) $< R_N$(tower).

Figure 7b and Table 3 show that $\Phi$(satellite) $\approx 0.90\Phi$(tower) suggesting a slight compensation for the underspecification of $R_{S\downarrow}$ through the underspecification of G from the satellite data. However, this evaluation assumes the energy balance to be closed in the tower data (i.e. $R_N$ - G = $\lambda$E + H), which typically is not the case, $\lambda$E + H often falling short of $R_N$ - G by 20 percent (Wilson et al., 2002). Because the causes of this energy imbalance remain controversial (see Foken, 2008 for review), it is difficult to estimate how much the tower values of $\lambda$E + H are actually biased low and hence the extent to which this bias affects our evaluation. Stoy et al. (2013) recently found a systematic relationship of the surface energy balance closure with landscape heterogeneity over 173 FLUXNET tower sites and reported an energy imbalance of 9 − 30 percent over diverse biomes. In another study, Amiro et al. (2009) found relatively better fulfilment of energy balance closure by averaging data over longer periods. The monthly averages of (AIRS overpass time) 13:30 hours surface energy balance closure of the 30 sites used here (Table 5) shows an average energy imbalance of ~20 percent (ranging from 8 to 34

19

520    percent). The errors in the tower data are also believed to be associated with different footprint characteristics for the different instruments used (Lin et al., 2008). For example, $R_N$ observations typically have a footprint size of ~10 m$^2$ whilst air properties (e.g. air temperature, humidity) have footprint sizes of > 1 km$^2$. By way of illustration, if, in the worst case, the entire energy imbalance was to be attributed exclusively to $\lambda E + H$ (i.e.

525    $R_N$ - G are quantified correctly), then the true midday $\lambda E + H$ could be some 20 percent greater (Wilson et al., 2002). As a result, the present bias seen in Table 3 would change to $\Phi(satellite) \approx 0.72\Phi(tower)$ again implicating $R_{S\downarrow}$ as the main source of bias in the satellite retrievals for both $R_N$ and $\Phi$.

We have only evaluated the satellite retrievals using data from terrestrial sites, and

530    clearly it would be worthwhile repeating this for the ocean retrievals if possible. We have held back on this evaluation here because of the lack of an extensive network of instantaneous latent and sensible heat flux or radiative flux data over the oceans, although we note that the SEAFLUX project within the Global Energy and Water Experiment (GEWEX) initiative should give rise to such a database in the near future. From the

535    terrestrial evaluation we would argue that the methodology employed here shows promise for specifying both noontime $R_N$ and $\Phi$, although the results suggests the need for improvements particularly in the specification of $R_{S\downarrow}$. More detailed studies evaluating the representativeness of each tower site footprint in relation to the 1° scale within which it is situated could prove useful in this regard as would methods for cloud-

540    proofing the satellite retrievals under persistent cloudy sky conditions. Similarly, evaluation under extreme conditions (e.g. high altitudes and latitudes) is also required.

## 5 Conclusions

We have demonstrated a novel retrieval for midday (13:30 hour) surface net available energy ($\Phi$) by blending the monthly atmospheric and land surface variables of AIRS and MODIS sensors. We have attempted to structure the method such that the $\Phi$ retrieval

545    does not depend on any offline calibration. We performed a two-step evaluation of the retrieved values for $\Phi$ at some representative surface radiation measurement sites and also over 30 FLUXNET sites from all over the globe.

Current $\Phi$ estimates performed well when compared against high spatio-temporal in situ measurements and coarse spatial resolution satellite retrievals. Consistent underestimation of $R_N$ was noted due to the underestimation of shortwave radiation and in tropical latitudes the $R_N$ (and $\Phi$) agreement was relatively weaker. Combination of high frequency cloud dynamics and relatively low seasonal variability of $R_{S\downarrow}$ makes it difficult to accurately model both $\Phi$ and $R_N$. One of the key challenges in modeling $R_N$ (and $\Phi$) in the tropics are to account for fast changing cloud cover fraction and cloud optical properties throughout the day.

With the availability of high spatial resolution (1 – 5 km) MODIS day-night optical and thermal data, our present approach could be extended to derive high spatial resolution $\Phi$ estimates at the global scale. This could be achieved by estimating MODIS-based day-night $R_N$ and combining day-night $R_N$ with day-night $T_S$ observations. At the same time, the current methodology could also be used on high temporal frequency observations of geostationary satellite (e.g., GOES and METEOSAT). Having estimated surface heat uptake and heat capacity (through equation 10), hourly G and $\Phi$ could be determined from hourly $R_N$ and $T_S$ observations of geostationary satellite by assuming conservation of heat capacity over a particular day. Operational generation of satellite based $\Phi$ product would be a valuable resource for a variety of investigations such as estimating latent and sensible heat, evaluation of Earth system model outputs, and quantifying the land-atmosphere coupling strength. Given we have resorted to the minimal amount of calibration in deriving $\Phi$ it would appear sensible if a similar philosophy were adopted in developing satellite-based schemes for latent and sensible heat fluxes as proposed in M2.

In addition to opportunities in specifying large scale surface heat and water vapor fluxes, the heat capacity estimates made here clearly carry information on variations in terrestrial properties such as surface moisture storage and we envisage that studies to develop this concept further could prove fruitful, particularly because of the emergence of satellite microwave data against which the results could be compared.

21

## Acknowledgments

## References

Adhikari, L., Wang, Z., and Whiteman, D.: Cloudy Assessment within an Atmospheric Infrared Sounder Pixel by Combining Moderate Resolution Spectroradiometer and Atmospheric Radiation Measurement Program Ground-Based Lidar and Radar Measurements, Sixteenth ARM Science Team Meeting Proceedings, Albuquerque, NM, March 27 - 31, 2006.

Amiro, B. D.: Measuring boreal forest evapotranspiration using the energy balance residual, J. Hydrol., 366, 112 – 118, 2009.

Ammann, C., Flechard, C. R., Leifeld, J., Neftel, A., Fuhrer, J.: The carbon budget of newly established temperature grassland depends on management intensity, Agric. Ecosys. Environ., 121, 5 20, 2007.

Anderson, M. C., Allen, R. G., Morse, A., and Kustas, W. P.: Use of Landsat thermal imagery in monitoring evapotranspiration and managing water resources, Remote Sens. Environ., 122, 50–65, 2012.

Anthoni, P. M., Knohl, A., Rebmann, C., Freibauer, A., Mund, M., Ziegler, W., Kolle, O., and Schulze, E. D.: Forest and agricultural land-use-dependent $CO_2$ exchange in Thuringia, Germany, Global Change Biol., 10 (12), 2005-2019, 2004.

Aubinet, M., Chermanne, B., Vandenhaute, M., Longdoz, B., Yernaux, M., and Laitat, F.: Long term carbon dioxide exchange above a mixed forest in the Belgian Ardennes, Agric. For. Meteorol., 108, 293–315, 2001.

Aumann, H. H., Chahine, M. T., Gautier, C., Goldberg, M. D., Kalnay, E., McMillin, L. M., Revercomb, H., Rosenkranz, P. W., Smith, W. L., Staelin, D. H., Strow, L., L., and Susskind, J.: AIRS/AMSU/HSB on the aqua mission: design, science objectives,

data products and processing systems, IEEE Trans. Geosci. Remote Sens., 41 (2), 253 – 264, 2003.

Baker, J.M. and Baker, D. G.: Long-term ground heat flux and heat storage at a mid-latitude site, Climatic Change, 54, 295 – 303, 2002.

610    Baldocchi, D. D., Falge, E., Gu, L., Olson, R., Hollinger, D., Running, S., Anthoni, P., Bernhofer, C., Davis, K., Evans, R., Fuentes, J., Goldstein, A., Katul, G., Law, B., Lee, X., Malhi, Y., Meyers, T., Munger, W., Oechel, W., Paw U, K. T., Pilegaard, K., Schmid, H. P., Valentini, R., Verma, S., Vesala, T., Wilson, K., and Wofsy, S.: Fluxnet: a new tool to study the temporal and spatial variability of ecosystem-scale
615    carbon dioxide, water vapor, and energy flux densities, Bull American Met. Soc., 82 (11), 2415 – 3434, 2001.

Baldocchi, D. D., Xu, L. K., and Kiang, N.: How plant functional-type, weather, seasonal drought, and soil physical properties alter water and energy fluxes of an oak-grass savanna and an annual grassland, Agric. For. Meteorol., 123, 13-39, 2004.

620    Bastiaanssen, W.G.M., Menenti, M., Feddes, R.A., and Holtslag, A.A.M.: The Surface Energy Balance Algorithm for Land (SEBAL): Part 1 formulation, J. Hydrol., 212-213, 198 – 212, 1998.

Batra, N., Islam, S., Venturini, V., Bisht, G., and Jiang L.: Estimation and comparison of evapotranspiration from MODIS and AVHRR sensors for clear sky days over the
625    southern great plains, Remote Sens. Environ., 103, 1 – 15, 2006.

Betts, A. K., Ball, J. H., and Beljaars, A. C. M.: Comparison between the land surface response of the ECMWF model and the FIFE-1987 data, Quart. J. Royal Met. Soc., 119, 975 – 1001, 1993.

Bhattacharya, B.K., Mallick, K., Patel, N.K., Parihar, J.S.: Regional clear sky
630    evapotranspiration over agricultural land using remote sensing data from Indian geostationary meteorological satellite, J. Hydrol., 387, 65 – 80, 2010.

Bhattacharya, B.K., Mallick, K., Nigam, R., Dakore, K.K, Sheikh, A.M.: Efficiency based wheat yield prediction in a semi-arid climate using surface energy budgeting with satellite observations, Agric. For. Meteorol., 1394 - 1408, 2011.Bindi, M.,
635    Miglietta, F., and Zipoli, G.:, Different methods for separating diffuse and direct components of solar radiation and their application in crop growth models, Climate Res., 2, 47 – 54, 1992.

Bisht, G., Venturini, V., Islam, S., and Jiang, L.: Estimation of Net Radiation Using MODIS (Moderate Resolution Imaging Spectroradiometrer) Terra data for clear sky
640    days, Remote Sens. Environ., 97(1), 52-67, 2005.

Bisht, G. and Bras, R.: Estimation of net radiation from the MODIS data under all sky conditions: Southern Great Plains case study, Remote Sens. Environ., 114, 1522 – 1534, 2010.

23

Bisht, G. and Bras, R. L.: Estimation of net radiation from the Moderate Resolution
645      Imaging Spectroradiometer over the Continental United States, IEEE Trans. Geosci.
     Remote Sens., 49(6), 2448 - 2462, 201, doi:10.1109/TGRS.2010.2096227, 2011.

Bounoua, L., Hall, F.G., Sellers, P.J., Kumar, A., Collatz, G.J., Tucker, C.J., and Imhoff,
     M.L.: Quantifying the negative feedback of vegetation to greenhouse warming: A
     modeling approach, Geophys. Res. Lett., 37, L23701, doi:10.1029/2010GL045338,
650      2010.

Bowen, I.S.: The ratio of heat losses by conduction and by evaporation from any water
     surface, Phy. Rev., 27, 779–787, 1926.

Cai, G., Xue, Y., Hu, Y., Guo, J., Wang, Y., and Qi, S.: Quantitative study of net
     radiation from MODIS data in the lower boundary layer in Poyang Lake area of
655      Jiangxi Province, China, Int. J Remote Sens., 28 (19), 4381 – 4389, 2007.

Cano, D., Monget, J. M., Albuisson, M., Guillard, H., Regas, N., and Wald, L.: A method
     for the determination of the global solar radiation from meteorological satellite data,
     Sol. Energy, 37, 31 – 39, 1986.

Carswell, F. E., Costa, A.L., Palheta, M., Malhi, Y., Meir, P., Costa, J. D. R., Ruivo, M.
660      D., Leal, L. D. M., Costa, J. M. N., Clement, R. J., and Grace, J.: Seasonality in CO2
     and H2O flux at an eastern Amazonian rain forest, J. Geophys. Res.-Atmos., 107,
     D20, 8076, 2002.

Chen, M., Zhuang, Q., and He, Y.: An Efficient Method of Estimating Downward Solar
     Radiation Based on the MODIS Observations for the Use of Land Surface Modeling,
665      Remote Sens., 6, 7136-7157; doi:10.3390/rs6087136, 2014.

Chen, X., Huang, X., Loeb, N.G., and Wei, H.: Comparisons of Clear-Sky Outgoing Far-
     IR Flux Inferred from Satellite Observations and Computed from the Three Most
     Recent Reanalysis Products, J. Climate, 26(2), 478–494, doi:10.1175/JCLI-D-
     1200212.1, 2013.

670 Choudhury, B. J.: Relationships between vegetation indices, radiation absorption, and net
     photosynthesis evaluated by a sensitivity analysis, Remote Sens. Environ., 22, 209 –
     233, 1987.

Choudhury, B. J.: Estimating gross photosynthesis using satellite and ancillary data:
     approach and preliminary results, Remote Sens. Environ., 75, 1 – 21, 2001.

675 Cook, B. D., Davis, K. J., Wang, W., Desai, A., Berger, B. W., Teclaw, R. M., Martin, J.
     G., Bolstad, P. V., Bakwin, P. S., Yi, C., and Heilman, W.: Carbon exchange and
     venting anomalies in an upland deciduous forest in northern Wisconsin, USA, Agric.
     For. Meteorol., 126, 271 – 295, 2004.

Corbari, C., Sobrino, J. A., Mancini, M., and Hidalgo, V.: Land surface temperature
680      representativeness in a heterogeneous area through a distributed energy-water balance

24

model and remote sensing data, Hydrol. Earth Syst. Sci., 14, 2141-2151, doi:10.5194/hess-14-2141-2010, 2010.

de Araújo, A. C., Nobre, A. D., Kruijt, B., Elbers, J. A., Dallarosa, R., Stefani, P., von Randow, C., Manzi, A. O., Culf, A. D., Gash, J. H. C., Valentini, R., and Kabat. P.: Comparative measurements of carbon dioxide fluxes from two nearby towers in a central Amazonian rainforest: the Manaus LBA site. J. Geophys. Res. Atmos., 107(D20):8090., doi: 10.1029/2001JD000676, 2002.

Dubayah, R. and Loechel, S.: Modeling Topographic solar radiation using GOES data, J Appl. Meteorol., 36 (2), 141 − 154, 1997.

Fischer, M. L., Billesbach, D. P., Berry, J. A., Riley, W. J., and Torn, M. S.: Spatiotemporal variations in growing season exchanges of $CO_2$, $H_2O$, and sensible heat in agricultural fields of the Southern Great Plains, Earth Int., 11, 1 − 21, 2007.

Foken, T., Wimmer, F., Mauder, M., Thomas, C., and Liebethal, C.: Some aspects of the energy balance closure problem, Atmos. Chem. Phys. 6, 4395–4402, 2006.

Foken, T.: The energy balance closure problem: an overview, Ecol. Appl. 18, 1351 − 1367, 2008.

Fouquart, Y. and Bonnel, B.: Computations of solar heating of the earth's atmosphere: A new parameterization, Beitr. Phys. Atmos., 53, 35–62, 1980.

Gao, W., Coulter, R. L., Lesht, B. M., Qiu, J., and Wesely M. L.: Estimating clear-sky regional surface fluxes in the southern great plains atmospheric radiation measurement site with ground measurements and satellite observations, J. Appl. Meteorol., 37, 5 − 22, 1998.

Gao, J. and Wu, S.: Simulated Effects of Land Cover Conversion on the Surface Energy Budget in the Southwest of China, Energies, 7, 1251-1264, doi:10.3390/en7031251, 2014.

Gentine, P., Entekhabi, D., Chehbouni, A., Boulet, G., Duchemin, B., : Analysis of evaporative fraction diurnal behaviour. Agric. For. Meteorol., 143, 13 − 29, 2007.

Giambelluca, T. W., Hölscher, D., Bastos, T. X., Frazão, R. R., Nullet, M. A., and Zeigler, A. D.: Observations of albedo and radiation balance over postforest land surfaces in the eastern Amazon Basin, J. Clim., 10, 919 − 928, 1997.

Gilmanov, T. G., Soussana, J.F., Aires, L., Allard, V., Ammann, C., Balzarolo, M., Barcza, Z., Bernhofer, C., Campbell, C. L., Cernusca, A., Cescatti, A., Brown, J. C., Dirks, O. M., Dore, S., Eugster, W., Fuhrer, J., Gimeno, C., Gruenwald, T., Haszpra, L., Hensen, A., Ibrom, A., Jacobs, A. F. G., Jones, M.B., Lanigan, G., Laurila, T., Ohila, A., Manca, G., Marcolla, B., Nagy, Z., Pilegaard, K., Pinter, K., Pio, C., Raschi, A., Rogiers, N., Sanz, M.J., Stefani, P., Sutton, M., Tuba, Z., Valentini, R., Williams, M. L., and Wohlfahrt, G.: Partitioning European grassland net ecosystem $CO_2$

exchange into gross primary productivity and ecosystem respiration using light response function analysis, Agric. Ecosys. Environ., (1-2), 93 – 120, 2007.

720 Goldstein, A. H., Hultman, N. E., Fracheboud, J. M., Bauer, M. R., Panek, J. A., Xu, M., Qi, Y., Guenther, A. B., and Baugh, W.: Effects of climate variability on the carbon dioxide, water, and sensible heat fluxes above a ponderosa pine plantation in the Sierra Nevada (CA), Agric. For. Meteorol., 101(2-3), 113 – 129, 2000.

Gough, C. M., Flower, C. E., Vogel, C. S. Dragoni, D., Curtis, P. S.: Whole-ecosystem
725 labile carbon production in a north temperate deciduous forest, Agric. For. Meteorol., 149, 1531 – 1540, 2009.

Goulden, M. L., Miller, S. D., and da Rocha, H. R., Menton, M. C., De Freitas, H. C., Figuera, A. M. E. S., and De Sousa, C. A. D.: Diel and seasonal patterns of tropical forest $CO_2$ exchange, Ecol. Appl., 14 (4), S42 – S54, 2004.

730 Granier, A., Loustau, D., and Breda, N.: A generic model of forest canopy conductance dependent on climate, soil water availability and leaf area index, Ann. For. Sc., 57 (8), 755 – 765, 2000a.

Granier, A., Biron, P., and Lemoine, D.: Water balance, transpiration and canopy conductance in two beech stands, Agric. For. Meteorol., 100 (4), 291 – 308, 2000b.

735 Gubler, S., Gruber, S., and Purves, R. S.: Uncertainties of parameterized surface downward clear-sky shortwave and all-sky longwave radiation, Atmos. Chem. Phys., 12, 5077-5098, doi:10.5194/acp-12-5077-2012, 2012.

Gueymard, C.: Direct solar transmittance and irradiance predictions with broadband models. Part I: detailed theoretical performance assessment, Sol. En., 74, 355 – 379,
740 2003.

Hammerle, A., Haslwanter, A., Tappeiner, U., Cernusca, A., and Wohlfahrt, G.: Leaf area controls on energy partitioning of a temperate mountain grassland, Biogeosci., 5, 421–431, 2008.

Hearty, T.J., Savtchenko, A., Tian, B., Fetzer, E., Yung, Y.L., Theobald, M., Vollmer, B.,
745 Fishbein, E., and Won, Y.: Estimating sampling biases and measurement uncertainties of AIRS/AMSU-A temperature and water vapor observations using MERRA reanalysis, J Geophys. Res. Atm., 119 (6), 2725–2741, DOI: 10.1002/2013JD021205, 2014.

Heitman, J.L., Horton, R., Sauer, T.J., Ren, T.S., and Xiao, X.: Latent heat in soil heat
750 flux measurements, Agric. For. Meteorol., 150, 1147 – 1153, 2010.

Hildebrandt, A., Aufi, M. A., Amerjeed, M., Shammas, M., and Eltahir, E. A. B.: Ecohydrology of a seasonal cloud forest in Dhofar: 1. Field experiment, Water Resourc. Res., 43, doi:10.1029/2006WR005261, 2007.

Hirano, T., Hirata, R., Fujinuma, Y., Saigusa, N., Yamamoto, S., Harazono, Y., Takada, M., Inukai, K., and Inoue, G.: $CO_2$ and water vapor exchange of a larch forest in northern Japan, Tellus B-Chem. Phys. Meteorol., 55, 244 – 257, 2003.

Hirano, T., Segah, H., Harada, T., Limin, S., June, T., Hirata, R., and Osaki, M.: Carbon dioxide balance of a tropical peat swamp forest in Kalimantan, Indonesia, Global Change Biol., 13, 412 – 425, 2007.

Hollinger, D. Y., Goltz, S. M., Davidson, E. A., Lee, J. T., Tu, K., and Valentine, H. T.: Seasonal patterns and environmental control of carbon dioxide and water vapour exchange in an ecotonal boreal forest, Global Change Biol., 5 (8), 891 – 902, 1999.

Hou, J., Jia, G., Zhao, T., Wang, H., and Tang, B.: Satellite based estimation of daily average net radiation under clear sky conditions, Adv. Atmos. Sci., 31, 705 – 720, 2014.

Huang, G. H., Liu, S. M., and Liang, S. L.: Estimation of net surface shortwave radiation from MODIS data, Int. J. Remote Sens., 33(3), 804-825, 2012.

Huang, G., Ma, M., Liang, S., Liu, S., and Li, X.: A LUT‑based approach to estimate surface solar irradiance by combining MODIS and MTSAT data, J. Geophys. Res., 116, D22201, doi:10.1029/2011JD016120, 2011.

Hwang K., Choi, M., Lee, S.O., and Seo, J.-W.: Estimation of instantaneous and daily net radiation from MODIS data under clear sky conditions: a case study in East Asia, Irrig. Sci., 31, 1173–1184, DOI 10.1007/s00271-012-0396-3, 2013.

Humes, K. S., Kustas, W. P., and Moran, M. S.: Use of remote sensing and reference site measurements to estimate instantaneous surface energy balance components over a semiarid rangeland watershed, Water Resour. Res., 30, 1363 – 1373, 1994.

Hutyra, L. R., Munger, J. W., Saleska, S. R., Gottlieb, E., Daube, B. C., Dunn, A. L., Amaral, D. F., de Camargo, P. B., and Wofsy, S. C.: Seasonal controls on the exchange of carbon and water in an Amazonian rain forest, J. Geophys. Res., 112, G03008, doi:10.1029/2006JG000365, 2007.

Hsieh C. I., Huang, C.W., and Kiely, G.: Long term estimation of soil heat flux by single layer soil temperature, Int. J. Biometeorol., 53, 113 – 123, 2009.

Jacobs, J. M., Anderson, M. C., Friess, L. C., and Diak, G. R.: Solar radiation, longwave radiation and emergent wetland evapotranspiration estimates from satellite data in Florida, USA, Hydrol. Sc., 49, 461 – 176, 2004.

Jaksic, V., Kiely G., Albertson J., Katul G., and Oren R.: Net ecosystem exchange of grassland in contrasting wet and dry years, Agric. For. Meteorol., 139(3-4): 323 – 334, 2006.

790      Jin, Z., Charlock, T. P., Smith Jr., W. L., and Rutledge, K.: A parameterization of ocean surface albedo, Geophys. Res. Let., 31, L22301, doi:10.1029/2004GL021180, 2004.

Jin, Y., Randerson, J. T., and Goulden, M. L.: Continental-scale net radiation and evapotranspiration estimated using MODIS satellite observations, Remote Sens. Environ., 115, 2302-2319, 2011.

795      Katul, G.G., Leuning, R., and Oren, R.: Relationship between plant hydraulic and biochemical properties derived from a steady-state coupled water and carbon transport model, Pl. Cell Environ., 26 (3), 339-350, 2003.

Kaufmann, Y.J. and Koran, I.: Smoke and Pollution Aerosol Effect on Cloud Cover, Science, 313, 655 – 658, 2006.

800      Kergoat, L., Grippa, M., Baille, A., Eymard, L., Lacaze, R., Mougin, E., Ottlé, C., Pellarin, T., Polcher, J. Rosnay, P.de., Roujean, J. -L., Sandholt, I., Taylor, C.M., Zin, I., Zribi, M.: Remote sensing of the land surface during the African Monsoon Multidisciplinary Analysis (AMMA), Atmos. Sci. Lett., 12, 129–134, 2011.

Kim, J. and Hogue, T.S., Evaluation of a MODIS-based potential evapotranspiration product at the point-scale, J. Hydrometeorol., 9 (3), 444–460, 2008.

805      Kustas, W. P. and Norman, J. M.: Evaluating the Effects of Subpixel Heterogeneity on Pixel Average Fluxes, Remote Sens. Environ., 74, 327 – 342, 2000.

Lakshmi, V. and Zehrfuhs, D.: Normalization and comparison of surface temperatures across a range of scales, IEEE Trans. Geosci. Remote Sens. 40 (12), 2636 – 2646, 2002.

810      Li, J. and Islam, S.: On the estimation of soil moisture profile and surface fluxes partitioning from sequential assimilation of surface layer soil moisture, J. Hydrol., 220, 86 – 103, 1999.

Liang, S., Strahler, A. H., and Walthall, C.: Retrieval of land surface albedo from satellite observations: A simulation study, J. of Appl. Meteorol., 38 (6), 712–725, 1999.

815      Liang, S., Shuey, C., Russ, A., Fang, H., Chen, M., Walthall, C., and Daughtry, C.: Narrowband to Broadband Conversions of Land Surface Albedo: II. Validation, Remote Sens. Environ., 84(1), 25-41, 2002.

Liang, X., Wood, E. F., Lettenmaier, D. P., Lohmann, D., Boone, A., Chang, S., Chen, F., Dai, Y., Desborough, C., Dickinson, R. F., Duan, Q., Ek, M., Gusev, Y. M., Habets, 820      F., Irannejad, P., Koster, R., Mitchell, K. E., Nasonova, O. N., Noilhan, J., Schaake, J., Schlosser, A., Shao, Y., Shmakin, A. B., Verseghy, D., Warrach, K., Wetzel, P., Xue, Y., Yang, Z. -L., and Zeng, Q.: The Project for Intercomparison of Land-surface Parameterization Schemes (PILPS) phase 2 (c) Red-Arkansas River basin experiment: 2. Spatial and temporal analysis of energy fluxes, Global and Planetary Change, 19, 825      137 – 159, 1998.

Lin, B., Stackhouse Jr., P. W., Minnis, P., Wielicki, B. A., Hu, Y., Sun, W., Fan, T. –F., and Hinkelman, L. M.: Assessment of global annual atmospheric energy balance from satellite observations, J Geophys. Res., 113, D16114, doi:10.1029/2008JD009869, 2008.

830    Liu, Z., Vavrus, S., He, F., Wen, N., and Zhong, Y.: Rethinking tropical ocean response to global warming: the enhanced equatorial warming, J. Clim., 18, 4684 – 4700, 2005.

Longman, R. J., Giambelluca, T. W., and Frazier, A. G.: Modeling clear-sky solar radiation across a range of elevations in Hawaiʻi: Comparing the use of input parameters at different temporal resolutions, J. Geophys. Res., 117, D02201, doi: 835    10.1029/2011JD016388, 2012.

Ma, Y., Su, Z., Li, Z., Koike, T., and Menenti, M.: Determination of regional net radiation and soil heat flux over a heterogeneous landscape of the Tibetan Plateau, Hydrol. Process., 16, 2963 – 2971, 2002.

Mallick, K., Bhattacharya, B. K., Rao, V. U. M., Reddy, D. R., Banerjee, S., Hoshali, V., 840    Pandey, V., Kar, G., Mukherjee, J., Vyas, S. P., Gadgil, A. S., and Patel, N. K.: Latent heat flux estimation in clear sky days over Indian agroecosystems using noontime satellite remote sensing data, Agric. For. Meteorol., 149 (10), 1646 – 1665, 2009.

Mallick, K., Jarvis, A.J., Boegh, E., Fisher, J.B., Drewry, D.T., Tu, K.P., Hook, S.J., Hulley, G., Ardo, J., Beringer, J., Arain, A., and Niyogi, D.: A surface temperature 845    initiated closure (STIC) for surface energy balance fluxes, Remote Sens. Environ., 141, 243 – 261, 2014a.

Mallick, K., Jarvis, A., Wohlfahrt, G., Kiely, G., Hirano, T., Miyata, A., Yamamoto, S., and Hoffmann, L.: Components of near-surface energy balance derived from satellite soundings – Part 2: Latent heat flux, Biogeosciences Discuss., 11, 8085-8113, 850    doi:10.5194/bgd-11-8085-2014, 2014b.

Mamadou, O., Cohard, J. M., Galle, S., Awanou, C. N., Diedhiou, A., Kounouhewa, B., and Peugeot, C.: Energy fluxes and surface characteristics over a cultivated area in Benin: daily and seasonal dynamics, Hydrol. Earth Syst. Sci., 18, 893-914, doi:10.5194/hess-18-893-2014, 2014.

855    Massaquoi, J.G.M.: Global solar radiation in Sierra Leone (West Africa), Solar and Wind Tech., 5 (3), 281 – 283, 1988.

Mayocchi, C. L. and Bristow, K. L.: Soil surface heat flux: some general questions and comments on measurements, Agric. For. Meteorol., 75, 43 – 50, 1995.

Mecikalksi, J.R., Diak, G. R., Anderson, M. C., and Norman, J. M.: Estimating fluxes on 860    continental scales using remotely-sensed data in an atmospheric-land exchange model, J. Appl. Meteorol., 35, 1352 – 1369, 1999.

29

Meyers, T. P. and Hollinger, S. E.: An assessment of storage terms in the surface energy balance of maize and soybean, Agric. For. Meteorol., 125 (1-2), 105 – 115, 2004.

865    Miglietta, F., Gioli, B., Brunet, Y., Hutjes, R. W. A., Matese, A., Sarrat, C., and Zaldei, A.: Sensible and latent heat flux from radiometric surface temperatures at the regional scale: methodology and evaluation, Biogeosc., 6, 1975 – 1986, 2009.

Mlawer, E. J., Taubman, S. J., Brown, P. D., Iacono, M. J. and Clough, S. A.: Radiative transfer for inhomogeneous atmosphere: RRTM, a validated correlated-k model for the longwave, J. Geophys. Res., 120D, 16663 – 16682, 1997.

870    Mlynczak, P.E., Smith, G.L., and Doelling, D.R.: The annual cycle of Earth radiation budget from Clouds and the Earth's Radiant Energy System (CERES) data, J Appl. Meteorol. Clim., 50, 2490 – 2503, DOI: 10.1175/JAMC-D-11-050.1, 2011.

Monteith, J. L.: Evaporation and environment, Symp. Soc. Exp. Biol., 19, 205 – 234, 1965.

875    Morcrette, J. J.: Assessment of the ECMWF model cloudiness and surface radiation fields at the ARM SGP site, Monthly Weather Rev., 130, 257 – 277, 2002.

Mu, Q., Heinsch, F. A., Zhao, M., and Running, S. W.: Development of a global evapotranspiration algorithm based on MODIS and global meteorology data, Remote Sens. Environ., 111, 519-536, 2007.

880    Mu, Q., Zhao M., and Running S. W.: Improvements to a MODIS Global Terrestrial Evapotranspiration Algorithm, Remote Sens. Environ., 115, 1781–1800, 2011.

Murray, T. and Verhoef, A.: Moving towards a more mechanistic approach in the determination of soil heat flux from remote measurements - I. A universal approach to calculate thermal inertia, Agric. For. Meteorol., 147 (1-2), 80-87, doi: 885    10.1016/j.agrformet.2007.07.004, 2007.

Niemela, S., Raisanen, P., and Savijarvi, H.: Comparison of surface radiative flux parameterizations Part I: Longwave radiation, Atmos. Res., 58, 1–18, 2001.

Ochsner, T.E., Sauer, T.J., and Horton, R.: Soil heat storage measurements in energy balance studies, Agron. J., 99, 311–319, 2007.

890    Oliphant, A. J., Spronken-Smith, R. A., Sturman, A. P., and Owens, I .F.: Spatial Variability of Surface Radiation Fluxes in Mountainous Terrain, J. Appl. Meteorol., 42, 113 – 128, 2003.

Peng, J., Liu, Y., Zhao, X., and Loew, A.: Estimation of evapotranspiration from MODIS TOA radiances in the Poyang Lake basin, China, Hydrol. Earth Syst. Sci., 17, 1431-895    1444, 2013.

Penman, H. L.: Natural evaporation from open water, bare soil and grass, Proc. Roy. Soc. London, A193, 120 – 145, 1948.

Pinker, R. T. and Laszlo, I.: Modeling Surface Solar irradiance for satellite applications on a global scale, J. Appl. Meteorol., 31(2), 194 – 211, 1992.

900   Prata, A.J.: A new long-wave formula for estimating downward clear-sky radiation at the surface, Q. J. R. Meteorol. Soc., 122, 1127 – 1151, 1996.

Priestley, K.J., Smith, G.L., Thomas, S., Cooper, D., Lee, R.B., Walikainen, D., Hess, P., Szewczyk, Z.P., and Wilson, R.: Radiometric Performance of the CERES Earth Radiation Budget Climate Record Sensors on the EOS Aqua and Terra Spacecraft
905   through April 2007, J. Atmos. Oceanic Technol., 28, 3–21, doi: http://dx.doi.org/10.1175/2010JTECHA1521.1, 2011.

Quaas, J., Stevens, B., Stier, P., and Lohmann, U.: Interpreting the cloud cover – aerosol optical depth relationship found in satellite data using a general circulation model, Atmos. Chem. Phys., 10, 6129–6135, 2010.

910   Reichstein, M., Tenhunen, J., Roupsard, O., Ourcival, J. M., Rambal, S., Miglietta, F., Peressotti, A., Pecchiari, M., Tirone, G., and Valentini, R.: Inverse modeling of seasonal drought effects on canopy $CO_2/H_2O$ exchange in three Mediterranean ecosystems, J. Geophys. Res.-Atmos., 108, D23, 2003.

Ryu, Y., Kang, S., Moon, S. K., and Kim, J.: Evaluation of land surface radiation balance
915   derived from moderate resolution imaging spectroradiometer (MODIS) over complex terrain and heterogeneous landscape on clear sky days, Agric. For. Meteorol., 148, 1538 – 1552, 2008.

Saigusa, N. Yamamoto, S., Murayama, S., Kondo, H., and Nishimura, N.: Gross primary production and net ecosystem exchange of a cool- temperate deciduous forest
920   estimated by the eddy covariance method, Agric. For. Meteorol., 112, 203 – 215, 2002.

Saito, M., Miyata, A., Nagai, H., and Yamada, T.: Seasonal variation of carbon dioxide exchange in rice paddy field in Japan, Agric. For. Meteorol., 135, 93 – 109, 2005.

Salomon, J. G., Schaff, C. B., Strahler, A. H., Gao, F., and Jin, Y. F.: Validation of the
925   MODIS bidirectional reflectance distribution function and albedo retrievals using combined observations from the Aqua and Terra platforms, IEEE Trans. Geosci. Remote Sens., 44 (6), 1555 – 1565, 2006.

Santanello, J. A. Jr. and Friedl, M. A.: Diurnal Covariation in Soil Heat Flux and Net Radiation, J. Appl. Meteorol., 42, 851 – 862, 2003.

930   Sauer, T.J., and Horton R.: Soil heat flux, In: Micrometeorology in Agricultural Systems (Eds. Hatfield, J.L., Baker, J.M.), American Society of Agronomy, Madison, Wisconsin, USA, pp. 131-154, 2005.

Scholes, R.J., Gureja, N., Giannecchinni, M., Dovie, D., Wilson, B., Davidson, N., Piggott, K., McLoughlin, C., van der Velde, K., Freeman, A., Bradley, S., Smart, R., and Ndala, S.:. The environment and vegetation of the flux measurement site near Skukuza, Kruger National Park, Koedoe, 44(1), 73 – 83, 2001.

Schwartz, S. E.: Heat capacity, time constant, and sensitivity of Earth's climate system, J. Geophys. Res., 112, D24S05, doi:10.1029/2007JD008746, 2007.

Seidel, F. C., Kokhanovsky, A. A., and Schaepman, M. E.: Fast and simple model for atmospheric radiative transfer, Atmos. Meas. Tech., 3, 1129-1141, doi:10.5194/amt-3-1129-2010, 2010.

Stackhouse, P. W., Gupta, S. K., Cox, S. J., Chiacchio, M., and Mikovitz, J. C.: The WCRP/GEWEX Surface Radiation Budget Project Release 2: An assessment of surface fluxes at 1° resolution. In: W.L. Smith and Y.M. Timofeyev, Editors, IRS 2000: Current problems in atmospheric radiation, International Radiation Symposium, St. Petersburg, Russia , 24 – 29, 2000.

Stephens, G.L., Wild, M., Stackhouse, P.W., L'Ecuyer, T., Kato, S., and Henderson, D.S.: The Global Character of the Flux of Downward Longwave Radiation, J. Climate, 25, 2329–2340, doi: http://dx.doi.org/10.1175/JCLI-D-11-00262.1, 2012.

Stisen, S., Sandholt, I., Nørgaard, A., Fensholt, R., and Jensen, K. H.: Combining the triangle method with thermal inertia to estimate regional evapotranspiration applied to MSG-SEVIRI data in the Senegal river basin, Remote Sens. Environ., 112, 1242 – 1255, 2008.

Stoy, P.C., Mauder, M., Foken, T., Marcolla, B., Boegh, E., Ibrom, A., Arain, M.A., Arneth, A., Aurela, M., Bernhofer, C., Cescatti, A., Dellwik, E., Duce, P., Gianelle, D., van Gorsel, E., Kiely, G., Knohl, A., Margolis, H., McCaughey, H., Merbold, L., Montagnani, L., Papale, D., Reichstein, M., Saunders, M., Serrano-Ortiz, P., Sottocornola, M., Spano, D., Vaccari, F., Varlagin, A.: A data-driven analysis of energy balance closure across FLUXNET research sites: The role of landscape scale heterogeneity, Agric. For. Meteorol., 171-172, 137-152, DOI: 10.1016/j.agrformet.2012.11.004, 2013.

Stramma, L., Cornillon, P., Weller, R. A., Price, J.F. and Briscoe, M.G. Large diurnal sea surface temperature variability: satellite and in situ measurements. J. Geophys. Res., 16, 827-837, 1986.

Sultan, S., Wu, R., and Ahmed, I..: Impact of Terrain and Cloud Cover on the Distribution of Incoming Direct Solar Radiation over Pakistan, Journal of Geographic Information System, 6 (1), 70 – 77, DOI:10.4236/jgis.2014.61008, 2014.

Sun, Z., Gebremichael, M., Wang, Q., Wang, J., Sammis, T. W., Nickless, A.: Evaluation of Clear-Sky Incoming Radiation Estimating Equations Typically Used in

970          Remote Sensing Evapotranspiration Algorithms, Remote Sens., 5, 4735-4752; doi:10.3390/rs5104735, 2013.

Tamai, K., Abe, T., Araki, M., and Ito, H.: Radiation budget, soil heat flux and latent heat flux at the forest floor in warm, temperate mixed forest, Hydrol. Proc., 12, 2105 – 2114, 1998.

975          Thornton, P. E. and Running, S. W.: An improved algorithm for estimating incident daily solar radiation from measurements of temperature, humidity, and precipitation, Agric. For. Meteorol., 93, 211 – 228, 1999.

Tittebrand, A. and Berger, F.H.: Spatial heterogeneity of satellite derived land surface parameters and energy flux densities for LITFASS-area, Atmos. Chem. Phys., 9, 980          2075–2087, 2009.

Trenberth, K., Fasullo, J., and Kiehl, J.: Earth's global energy budget, Bull. Amer. Meteor. Soc., 90, 311 – 323, http://dx.doi.org/10.1175/2008BAMS2634.1, 2009.

Trenberth, K.: Changes in precipitation with climate change, Clim. Res., 47, 123 – 138, doi: 10.3354/cr00953, 2011.

985          Urbanski, S., Barford, C., Wofsy, S. Kucharik, C., Pyle, E., Budney, J., Fitzjarrald, D., Czikowsky, M., and Munger, J. W.: Factors Controlling $CO_2$ Exchange at Harvard Forest on Hourly to Annual Time Scales, J. Geophys Res., 112, G02020, doi:10.1029/2006JG000293, 2007.

Verhoef, A., Ottle, C., Cappelaere, B., Murray, T., Saux-Picart, S., Zribi, M., Maignan, 990          F., Boulain, N., Demarty, J., and Ramier, D.: Spatio-temporal surface soil heat flux estimates from satellite data: results for the AMMA experiment at the Fakara (Niger) supersite, Agric. For. Meteorol., 154-155, 55-66, doi: 10.1016/j.agrformet.2011.08.003, 2012.

Verstraeten W., Veroustraete, F., and Feyen, J.: Estimating evapotranspiration of 995          European forests from NOAA-imagery at satellite overpass time: Towards an operational processing chain for integrated optical and thermal sensor data products, Remote Sens. Environ., 96 (2), 256-276, 2005.

Wang, H. and Pinker, R. T., Shortwave radiative fluxes from MODIS: Model development and implementation, J. Geophys. Res., 114, D20201, 2009. 1000         doi:10.1029/2008JD10442.

Wielicki, B. A., Barkstrom, B. R., Baum, B. A., Charlock, T. P., Green, R. N., Kratz, D. P., Lee, R. B., Minnis, P., Smith, G. L., Wong, T. M., Young, D. F., Cess, R. D., Coakley, J. A., Crommelynck, D. A. H., Donner, L., Kandel, R., King, M. D., Miller, A. J., Ramanathan, V., Randall, D. A., Stowe, L. L., and Welch, R. M.: Clouds and the 1005         Earth's Radiant Energy System (CERES): Algorithm overview, IEEE Trans. Geosc. Remote Sens., 36(4), 1127 – 1141, 1998.

Wild, M., Folini, D., Schar, C., Loeb, N., Dutton, E.G., Langlo, G.K.: The global energy balance from a surface perspective, Clim. Dyn., 40, 3107–3134, DOI 10.1007/s00382-012-1569-8, 2013.

1010  Wilson, K. B., Goldstein, A. H., Falge, E., Aubinet, M., Baldocchi, D., Berbigier, P., Bernhofer, Ch., Ceulemans, R., Dolman, H., Field, C., Grelle, A., Law, B., Meyers, T., Moncrieff, J., Monson, R., Oechel, W., Tenhunen, J., Valentini, R., and Verma, S.: Energy balance closure at FLUXNET sites, Agric. Forest Meteorol., 113, 223-243, 2002.

1015  Wright, I. R., Gash, J. H. C., da Rocha, R., Shuttleworth, W. J., Nobre, C. A., Maitelli, G. T., Zamparoni, C. A. G. P., and Carvalho, P. R. A.: Dry season micrometeorology of central Amazonian ranchland, Q. J. R. Meteorol. Soc., 118, 1083 – 1099, 1992.

Zhang, J. H., Han, S. J., and Yu, G. R.: Seasonal variation in carbon dioxide exchange over a 200-year-old Chinese broad-leaved Korean pine mixed forest, Agric. For.
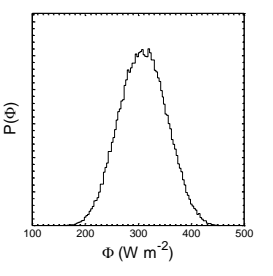1020  Meteorol., 137, 150 – 165, 2006.

1025

1030

34
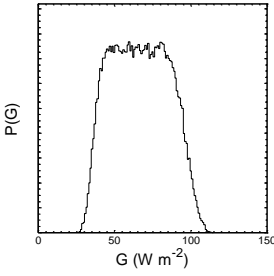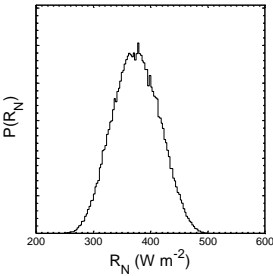
1035    **Table 1**. Eddy covariance sites used for the evaluation of the satellite derived $R_N$ and $\Phi$

| Biome type | Site name, Country | Latitude (°) | Longitude (°) | Reference |
|---|---|---|---|---|
| Evergreen broadleaf forest (EBF) | Palagkaraya, Indonasia | -2.35 | 114.04 | Hirano et al. (2007) |
| | Puechabon, France | 43.74 | 3.6 | Reichstein et al. (2003) |
| | Caxiuana Forest-Almeirim, Brazil | -1.72 | -51.46 | Carswell et al. (2002) |
| | Manaus - ZF2 K34, Brazil | -2.61 | -60.21 | de Araújo et al. (2004) |
| | Santarem-Km67, Brazil | -2.86 | -54.96 | Hutyra et al. (2007) |
| | Santarem-Km83, Brazil | -3.02 | -54.58 | Goulden et al. (2004) |
| Mixed forest (MF) | Vielsalm, Belgium | 50.31 | 5.99 | Aubinet et al. (2001) |
| | Tomakomai National forest, Japan | 42.73 | 141.52 | Hirano et al. (2003) |
| | Changbaishan, China | 42.4 | 128.09 | Zhang et al. (2006) |
| Grassland (GRA) | Oensingen1 grass, Switzerland | 47.29 | 7.73 | Ammann et al. (2007) |
| | Neustift/Stubai Valley, Austria | 47.12 | 11.32 | Hammerle et al. (2008) |
| | Goodwin Creek, USA | 34.25 | -89.87 | Unpublished |
| | Bugacpuszta, Hungary | 46.69 | 19.61 | Gilmanov et al. (2007) |
| | Dripsey, Ireland | 51.99 | -8.75 | Jaksic et al. (2006) |
| Cropland (CRO) | ARM Southern Great Plains, USA | 36.61 | -97.49 | Fischer et al. (2007) |
| | Bondville, USA | 40.01 | 88.29 | Meyers et al. (2004) |
| | Tsukuba, Japan | 36.05 | 140.03 | Saito et al. (2005) |
| Evergreen needleleaf forest (ENF) | Le Bray, France | 44.72 | -0.77 | Granier et al. (2000a) |
| | Duke Forest - loblolly pine, USA | 35.98 | -79.09 | Katul et al. (2003) |
| | Blodgett forest, USA | 38.89 | -120.63 | Goldstein et al. (2000) |
| | Howland forest, USA | 45.2 | -68.74 | Hollinger et al. (1999) |
| Deciduous broadleaf forest (DBF) | Harvard Forest EMS Tower (HFR1), USA | 42.54 | -72.17 | Urbanski et al. (2007) |
| | Univ. of Michigan Biological Station, USA | 45.56 | -84.71 | Gough et al. (2009) |
| | Willow Creek, USA | 45.81 | -90.08 | Cook et al. (2004) |
| | Hesse Forest- Sarrebourg, France | 48.67 | 7.06 | Granier et al. (2000b) |
| | Hainich, Germany | 51.08 | 10.45 | Anthoni et al. (2004) |
| | Morgan Monroe State forest, USA | 39.32 | -86.41 | Baldocchi et al. (2001) |
| | Takayama, Japan | 36.15 | 137.42 | Saigusa et al. (2002) |
| Savanna (SAV) | Tonzi Ranch, USA | 38.43 | -120.97 | Baldocchi et al. (2004) |
| | Skukuza, South Africa | -25.02 | 31.49 | Scholes et al. (2001) |

35

1040 **Table 2.** Sensitivity analysis results. The forcing data are taken for mid-summer on the Southern Great Plains, US. Sensitivities are locally linear, averaged across the ensemble response and expressed as dimensionless relative changes. Only absolute sensitivities > 0.1 are shown. $N = 10^5$ realisations.

| x | sample range | G (W m$^{-2}$) | R$_N$ (W m$^{-2}$) | Φ (W m$^{-2}$) |
|---|---|---|---|---|
| | | dG/dx | dR$_N$/dx | dΦ/dx |
| $\tau_A$ | ±10 % | - | 1.30 | 1.58 |
| f | ±10 % | - | -0.77 | -0.94 |
| α | ±10 % | - | -0.25 | -0.31 |
| $\varepsilon_S$ | ±10 % | 1.00 | -0.31 | -0.37 |
| $\varepsilon_C$ | ±10 % | -4.60 | 0.98 | 1.19 |
| $T_S$ | ±1 K | 0.75 | -0.17 | -0.21 |
| $T_{1000}$ | ±1 K | -0.33 | - | - |
| | |  |  |  |
| **standard deviation** | | 18 W m$^{-2}$ | 40 W m$^{-2}$ | 44 W m$^{-2}$ |

36

**Table 3**. Comparative statistics for the satellite and tower derived monthly midday (13:30 hour) $R_N$ and $\Phi$ for a range of biomes. Values in parenthesis are ±one standard deviation.

| Biome | **$R_N$** | | | | | **$\Phi$** | | | | |
|---|---|---|---|---|---|---|---|---|---|---|
| | RMSD (Wm$^{-2}$) | Gain | Offset | r | N | RMSD (Wm$^{-2}$) | Gain | Offset | r | N |
| EBF | 126.67 | 0.58 (±0.08) | 107.45 (±39.93) | 0.65 (±0.09) | 69 | 87.67 | 0.66 (±0.08) | 108.71 (±32.10) | 0.70 (±0.09) | 65 |
| MF | 104.21 | 0.82 (±0.07) | -32.40 (±23.73) | 0.89 (±0.08) | 36 | 87.29 | 0.97 (±0.10) | -65.25 (±27.07) | 0.86 (±0.09) | 32 |
| GRA | 74.29 | 0.73 (±0.05) | 51.37 (±15.88) | 0.88 (±0.06) | 59 | 61.51 | 0.83 (±0.07) | 15.71 (±16.21) | 0.86 (±0.07) | 53 |
| CRO | 89.13 | 0.73 (±0.08) | 35.62 (±28.57) | 0.84 (±0.09) | 36 | 53.31 | 0.99 (±0.10) | -0.23 (±23.98) | 0.87 (±0.09) | 36 |
| ENF | 85.45 | 0.87 (±0.04) | -26.83 (±14.78) | 0.96 (±0.04) | 48 | 66.7 | 1.01 (±0.05) | -56.56 (±15.27) | 0.95 (±0.05) | 46 |
| DBF | 92.77 | 0.71 (±0.05) | 21.74 (±15.15) | 0.85 (±0.06) | 84 | 71.57 | 0.88 (±0.06) | -16.70 (±14.23) | 0.85 (±0.06) | 80 |
| SAV | 103.98 | 0.69 (±0.08) | 56.28 (±36.08) | 0.87 (±0.11) | 23 | 61.98 | 0.97 (±0.11) | -14.42 (±37.68) | 0.88 (±0.25) | 23 |
| Pooled | 98.21 (28%) | 0.75 (±0.02) | 23.37 (±8.20) | 0.88 (±0.03) | 355 | 72.26 (22%) | 0.90 (±0.03) | -2.43 (±8.19) | 0.87 (±0.03) | 335 |

N = number of data points falling under individual biomes. $\Phi = (H + \lambda E)$ (for the tower sites).

EBF = Evergreen broadleaf forest, MF = Mixed forest, GRA = Grassland, CRO = Cropland, ENF = Evergreen needleleaf forest, DBF = Deciduous broadleaf forest, SAV = Savanna

**Table 4**. Summary of errors and characteristics of some of the dedicated satellite based $R_N$ and $R_{S\downarrow}$ retrieval studies

| Radiative flux variables | Reference | Sensor used | Spatial resolution | Temporal resolution | RMSD (W m$^{-2}$) |
|---|---|---|---|---|---|
| $R_N$ | Verstraeten et al. (2005) | NOAA AVHRR | 1 km | Instantaneous | 5 - 45 |
| | Bisht et al. (2005) | MODIS Terra | 5 km | Instantaneous | 74 |
| | Cai et al. (2005) | MODIS Terra and Aqua synergie | 5 km | Instantaneous | 19 |
| | Bisht and Bras (2010) | MODIS Terra | 5 km | Instantaneous | 23 - 39 |
| | Hwang et al. (2013) | MODIS Terra | 5 km | Instantaneous | 58 - 142 |
| | Hou et al. (2014) | MODIS Terra | 5 km | Daily | 37 - 40 |
| | Bisht et al. (2005) | MODIS Terra | 5 km | Daily | 60 |
| | Peng et al. (2013) | MODIS Terra | 5 km | Daily | 33 |
| | Jin et al. (2013) | MODIS Terra | 5 km | Monthly average | 44 |
| | Mallick et al. (2014) (current study) | AIRS and MODIS Terra | 1 degree | Instantaneous monthly average | 74 - 126 |
| $R_{S\downarrow}$ | Chen et al. (2014) | MODIS Terra | 1 degree | Daily | 39 |
| | Sun et al. (2013) | In situ observations | Tower footprint | Instantaneous | 36 – 89 |
| | Huang et al. (2012) | MODIS Terra | 5 km | Instantaneous | 54 – 83 (in $R_{NS}$) |
| | Huang et al. (2011) | MODIS Terra | 5 km | Instantaneous | 60 – 137 |
| | Wang and Pinker (2009) | MODIS Terra and Aqua | 1 degree | Instantaneous | 77 – 158 |
| | Kim and Hogue (2008) | MODIS Terra | 5 km | Instantaneous | 76 |
| | Tang et al. (2006) | MODIS Terra | 5 km | Daily | 20 – 35 (in $R_{NS}$) |
| | Mallick et al. (2014) (current study) | AIRS | 1 degree | Instantaneous monthly average | 110 |

1075

1080 **Table 5**. The mean and standard deviation of monthly midday (13:30 hour) surface energy balance closure ($C_{EB}$) of different biome types for the 21 (out of 30) FLUXNET sites (N) under study. Nine out of 30 sites had missing ground heat flux. $C_{EB}$ is computed according to Stoy et al. (2013).

| Biome types | N | $C_{EB}$ |
|---|---|---|
| EBF | 2 | $0.92 \pm 0.15$ |
| MF | 3 | $0.76 \pm 0.12$ |
| GRA | 4 | $0.84 \pm 0.08$ |
| CRO | 3 | $0.77 \pm 0.10$ |
| ENF | 3 | $0.80 \pm 0.02$ |
| DBF | 4 | $0.66 \pm 0.05$ |
| SAV | 2 | $0.79 \pm 0.08$ |

1085

1090

1095

1100

1105

1110
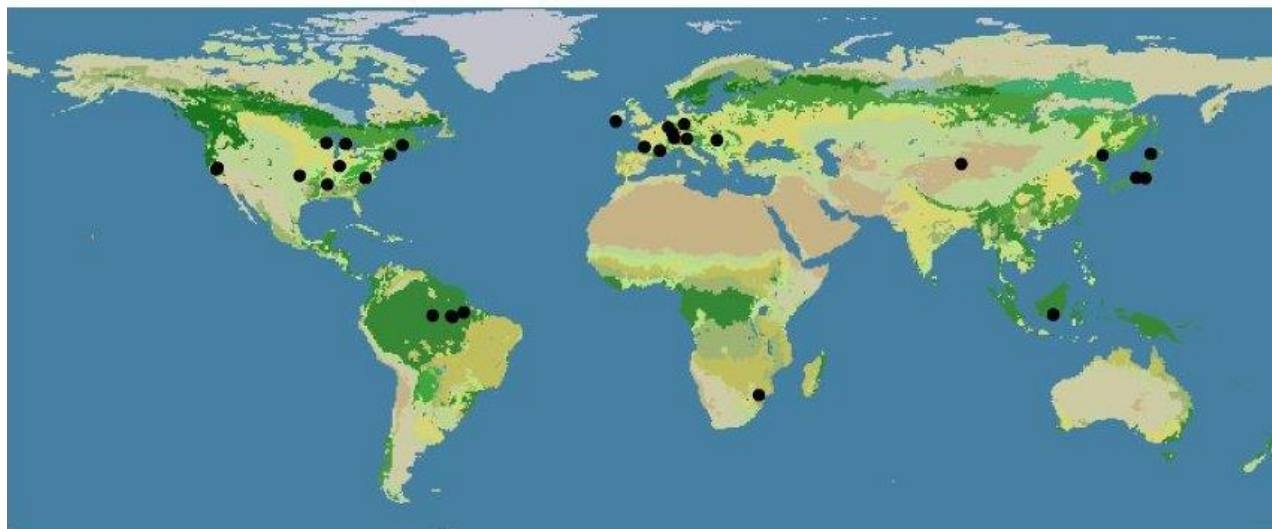
**Figure 1**. The distribution of the 30 eddy covariance tower sites used for evaluating $R_N$ and $\Phi$.

1115

1120

1125

1130
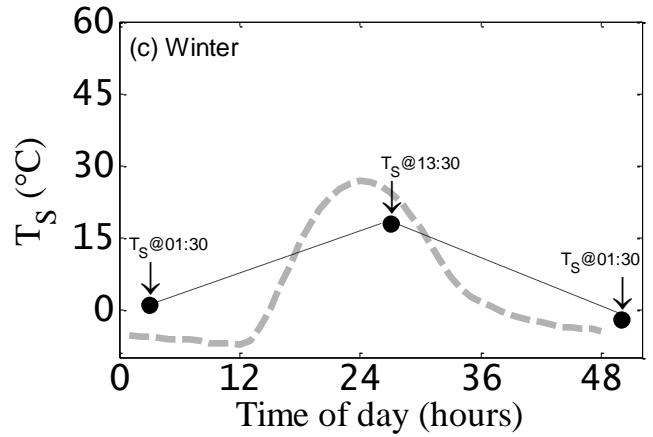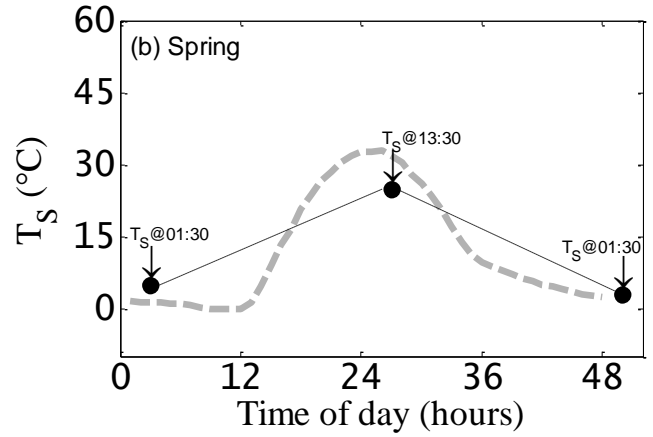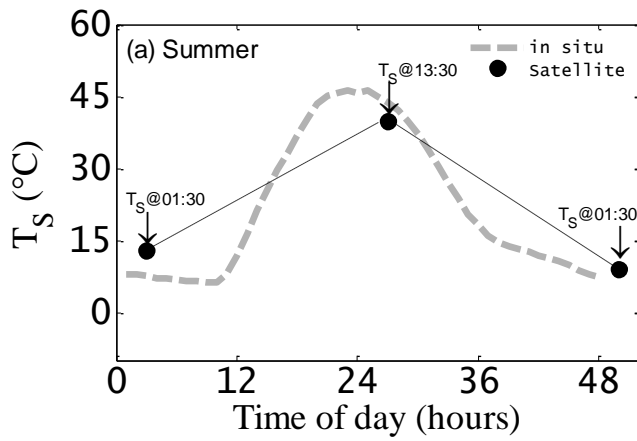
**Figure 2.** Illustrative examples of in situ monthly diurnal surface temperature ($T_S$) and the saw-tooth pattern of monthly satellite midday(13:30 hour) – night (1:30 hour) $T_S$ (as hypothesized in equation 10) for three different seasons of a year. This shows a linear rise and fall of day-night $T_S$ (dotted black line) or vice versa and indicates $\Delta T_S$ symmetry. This also shows how well the two $T_S$ samples capture the dynamic range of the day and hence the discretisation is representative of the daily energy balance.

1135

1140

1145

1150
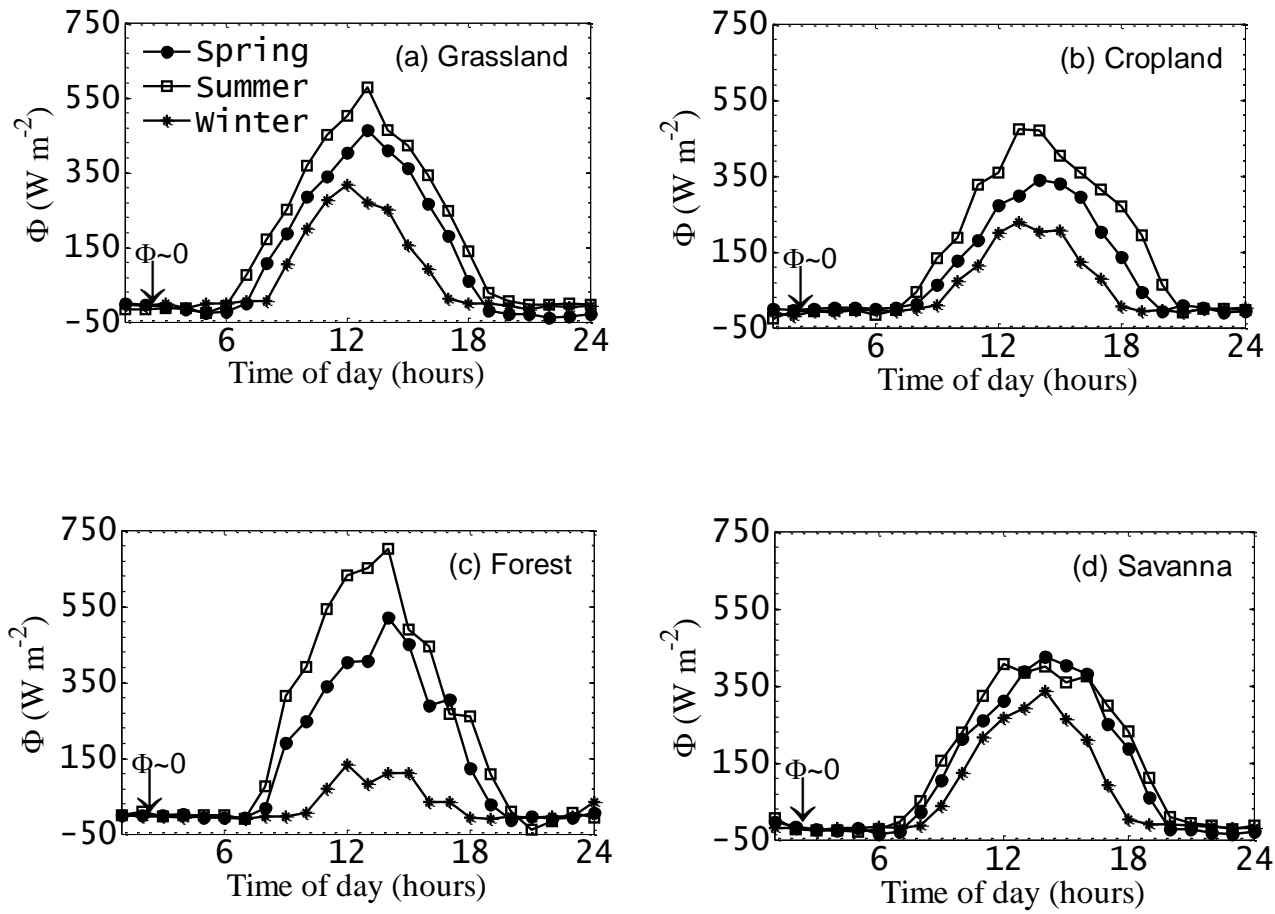
**Figure 3.** Examples of the diurnal evolution of net available energy ($\Phi$) ($=\lambda E + H$) during three different times of year over four representative biome types. This shows $\Phi \cong 0$ around 1:30 hours.
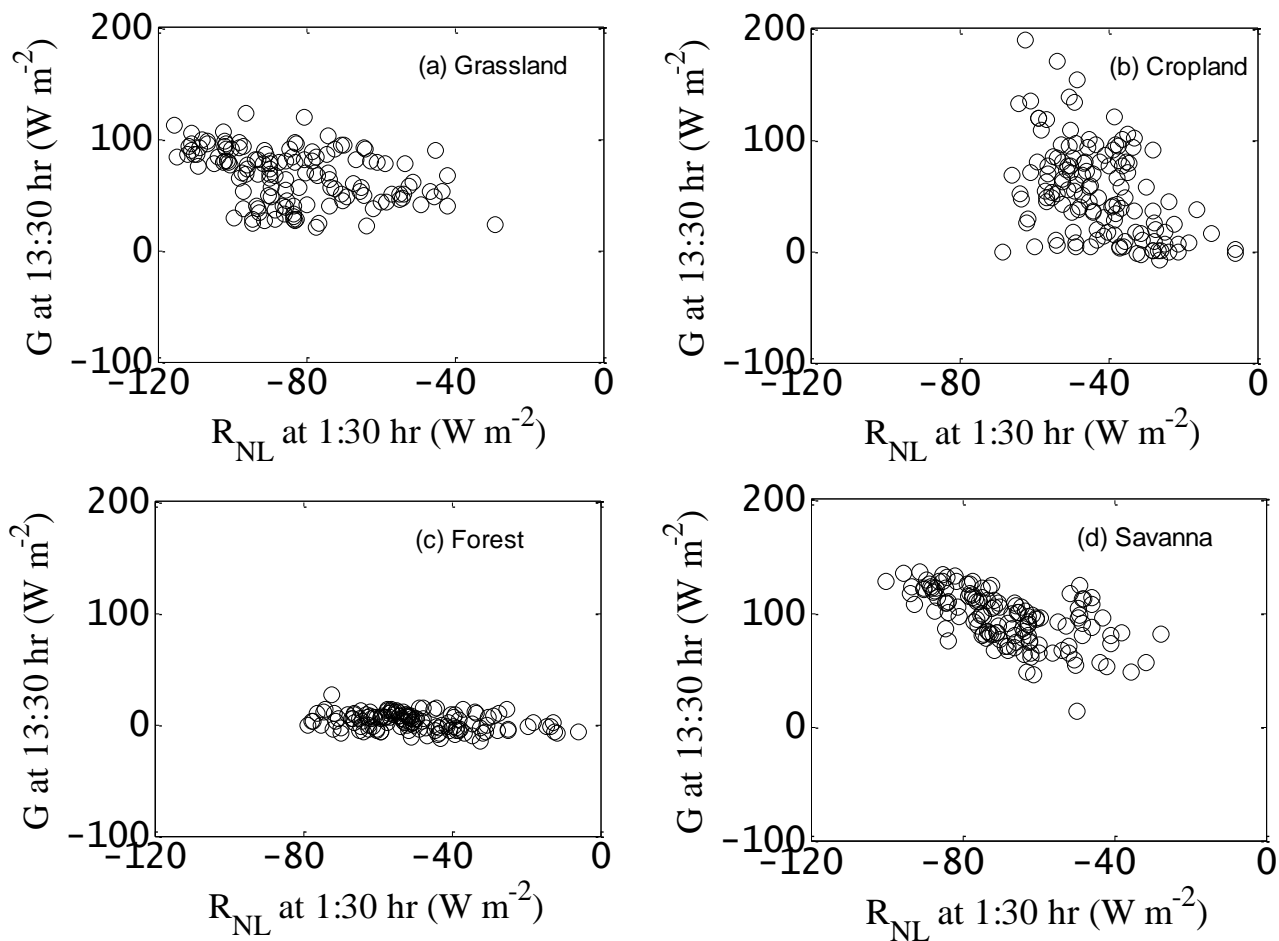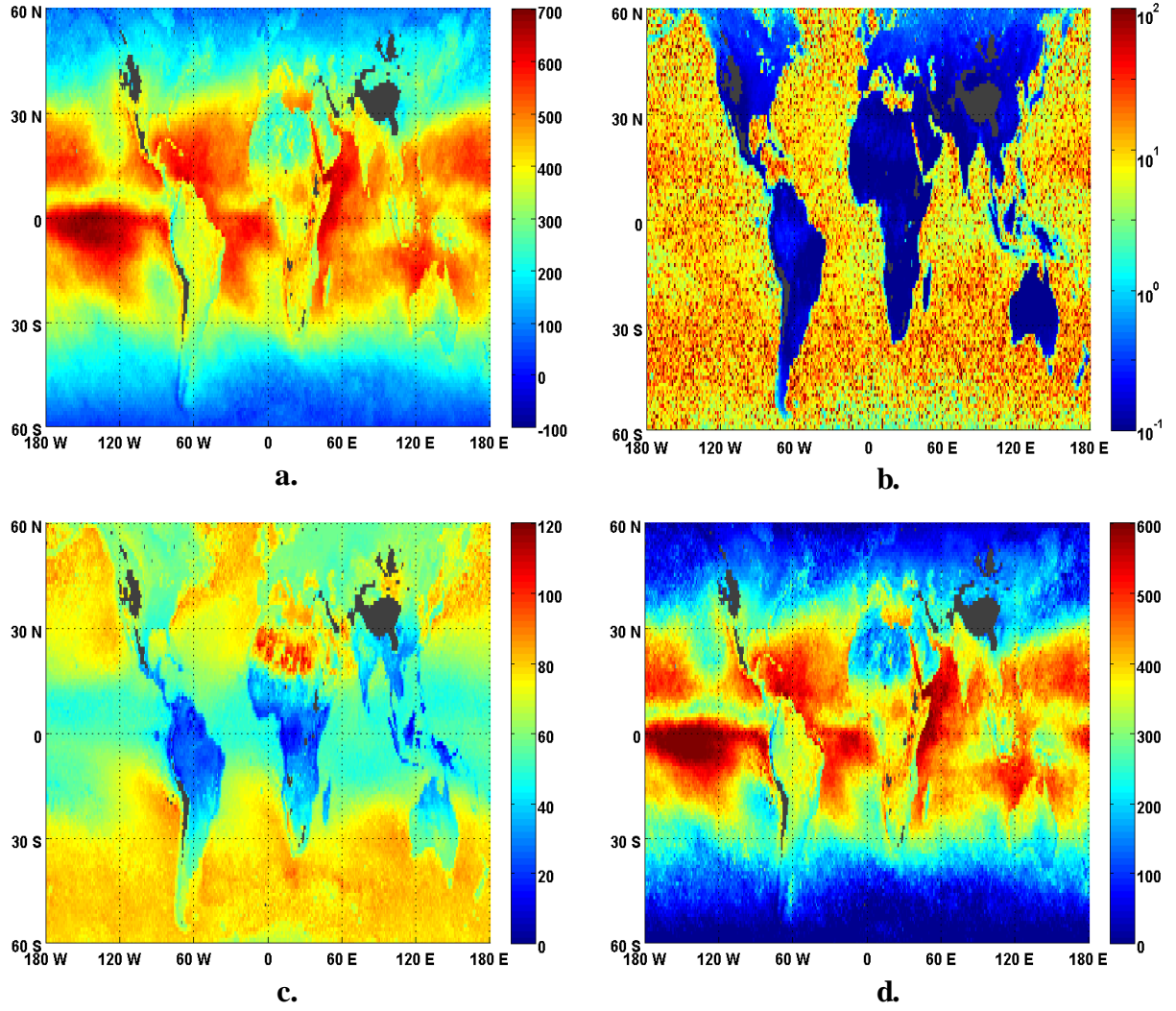
**Figure 4.** Observational relationship nighttime (1:30 hour) net longwave radiation ($R_{NL}$) and midday (13:30 hour) G measurements. Despite the scale mismatch between the two measurements, moderate (r = 0.32 - 0.44) (forest, cropland) to high (r = 0.60) (grassland and savanna) relationship is notable.

1175

1180

1185

**Figure 5.** Global fields for annual average 13:30 hour: **a.** net radiation $R_N$ (W m$^{-2}$); **b.** Surface heat capacity, c (MJ m$^{-2}$ K$^{-1}$); **c.** surface heat accumulation rate, G (W m$^{-2}$); **d.** net available energy, $\Phi$ (W m$^{-2}$), for 2003.

44

1195
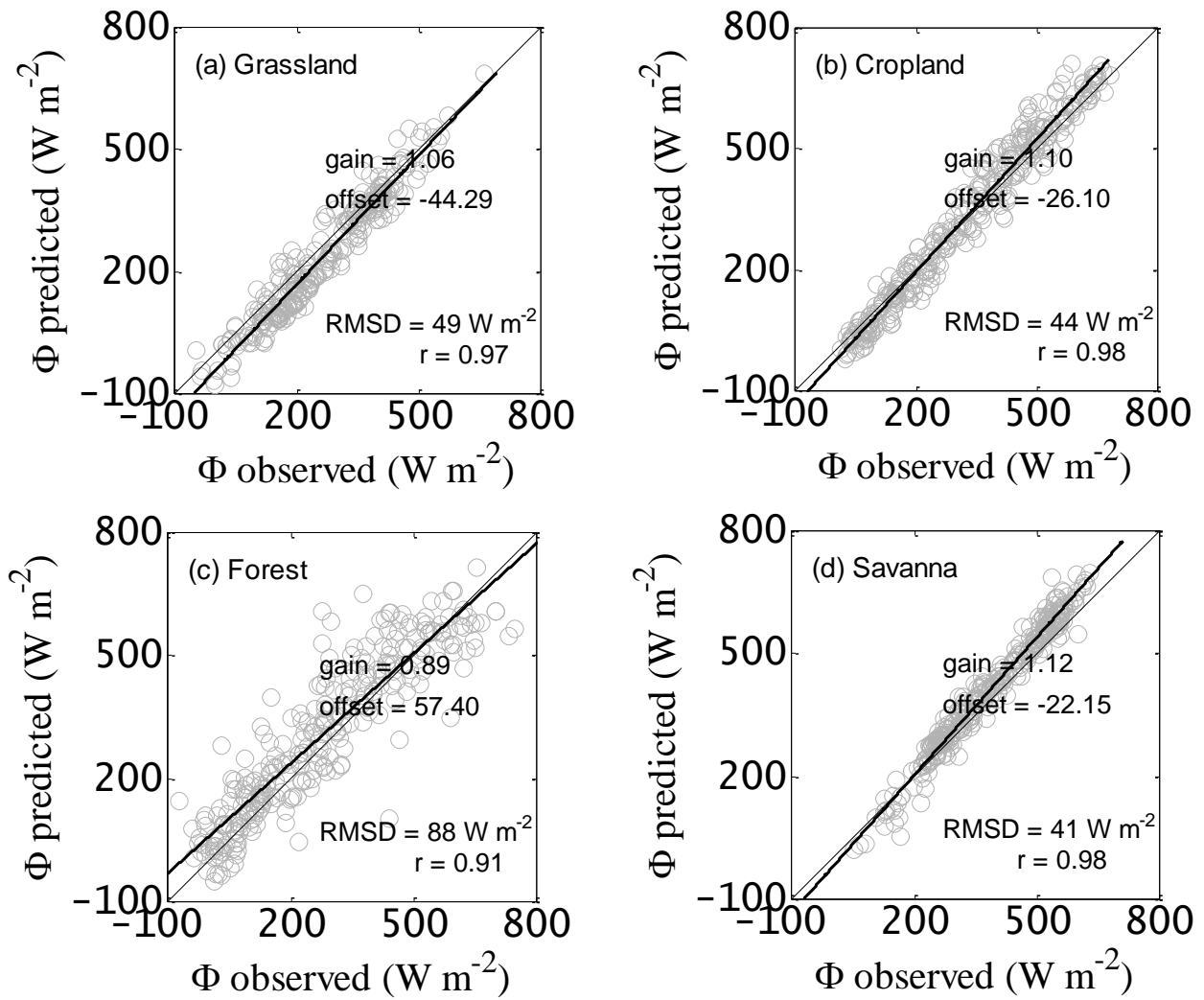


**Figure 6.** Validation of net available energy ($\Phi$)(=$\lambda$E + H)using high temporal frequency (daily) observations of midday (13:30 hour) and night (1:30 hour) $R_N$ and $T_S$ (solving equations 10a and 10b) at the eddy covariance tower sites over four representative biomes.
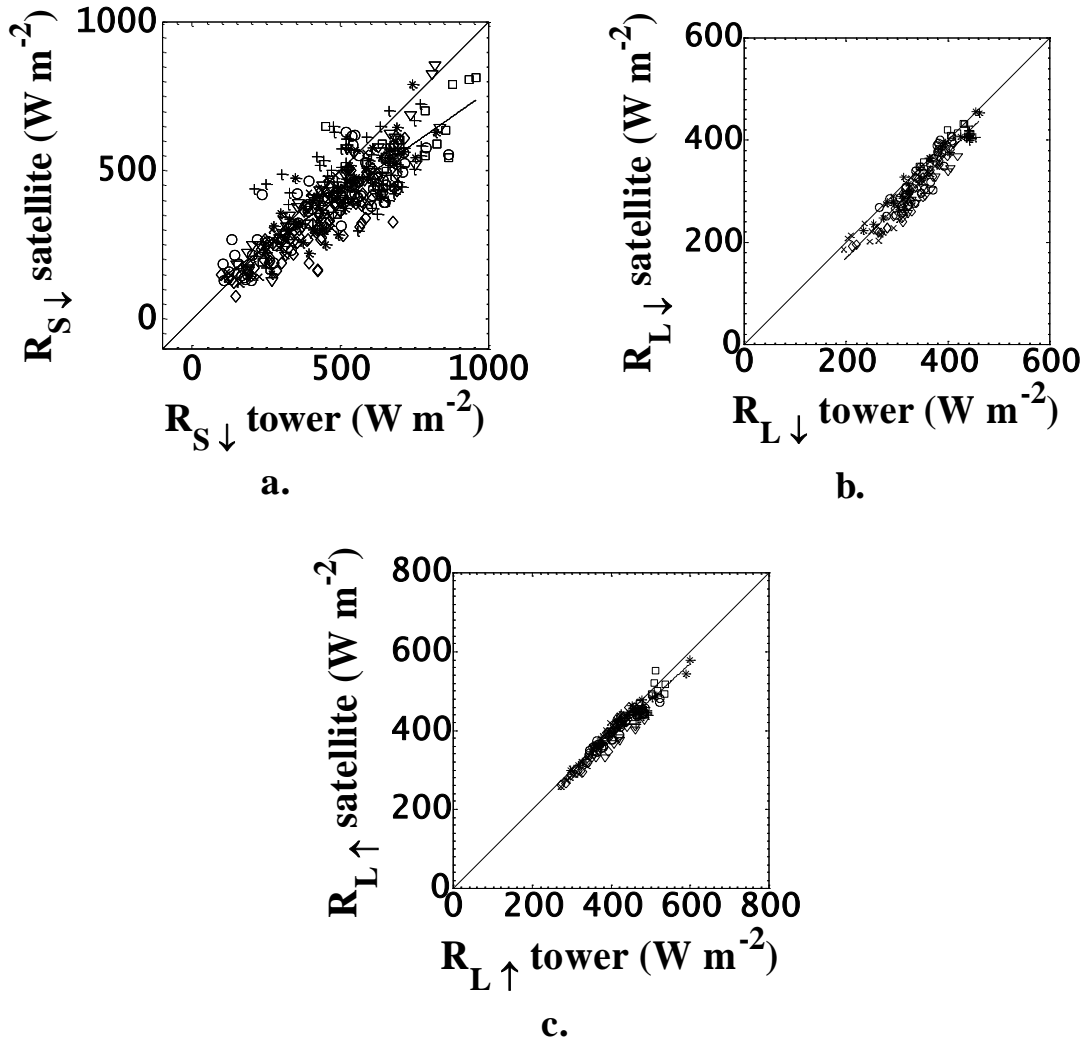
1200

**a.**                                 **b.**
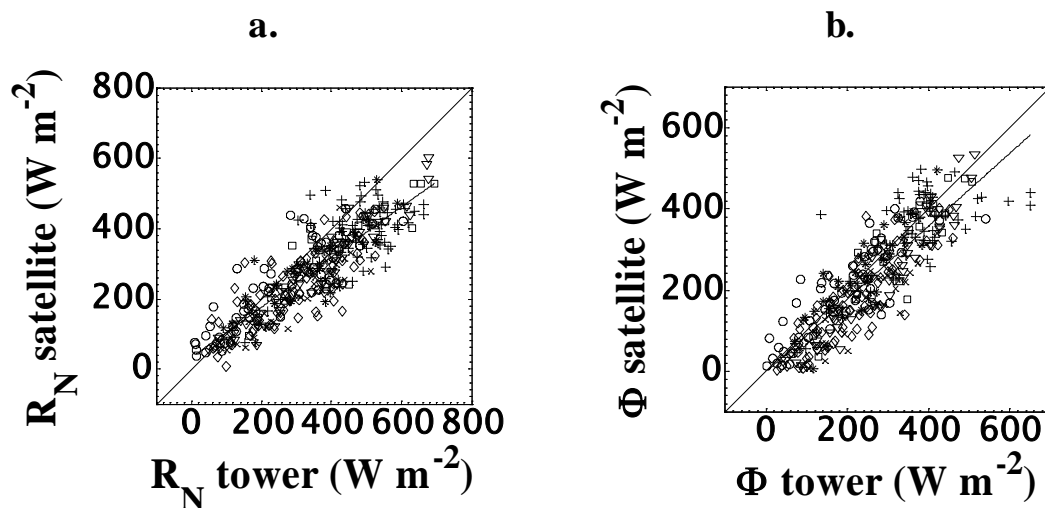


**Figure 7.** Comparison of satellite and tower monthly average 13:30 hour **a.** $R_N$. and **b**. $\Phi$ [$\Phi = (H + \lambda E)$ (for the tower sites)]. For details of the site characteristics see Table 1. For the comparative statistics see Table 3. The solid line is the pooled linear regression given in Table 3.

(+ EBF; x MF; ○ GRA; * CRO; ∇ ENF; ◊ DBF; □ SAV)
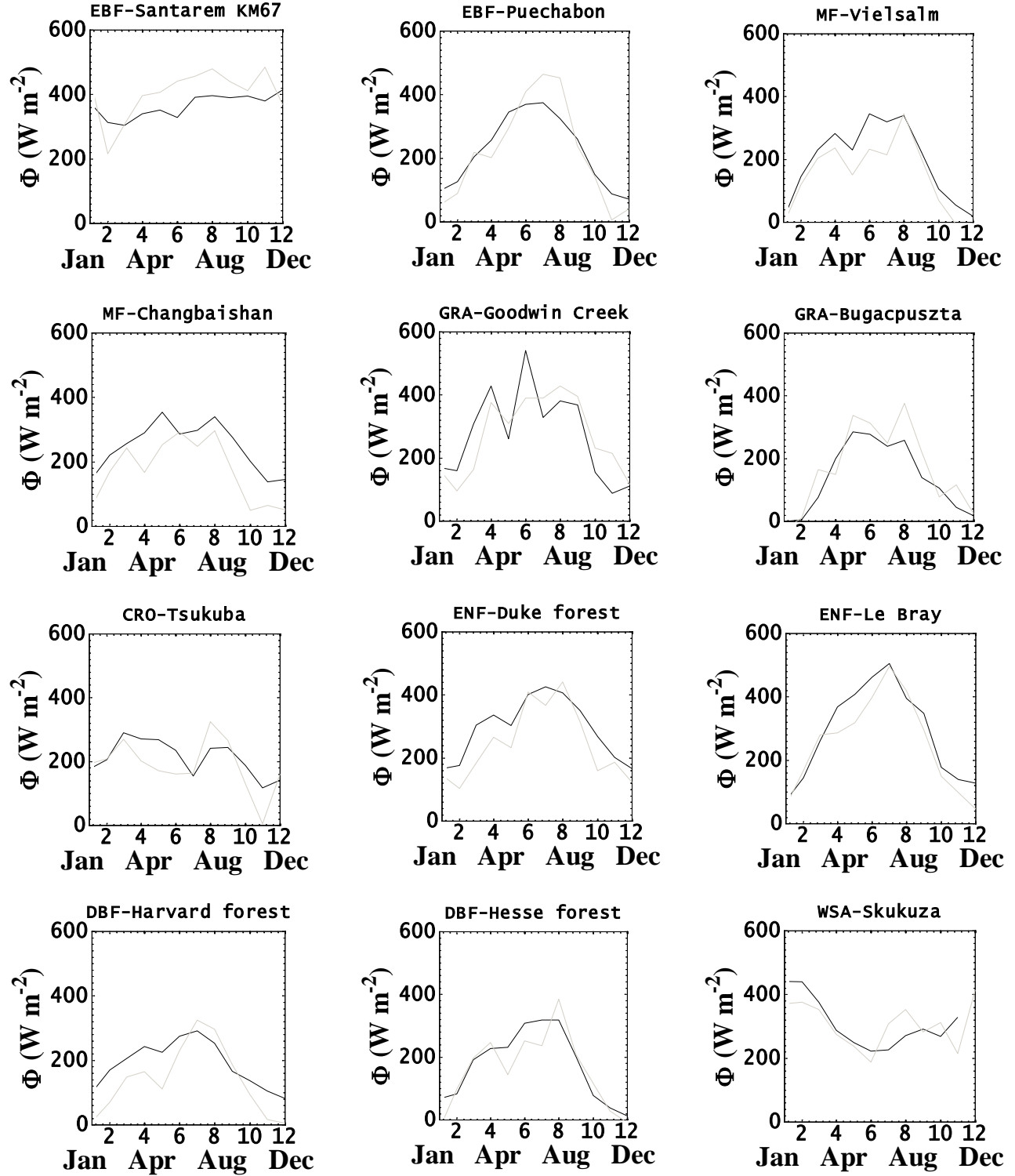
**Figure 8.** Satellite (grey) and tower (black) time series of monthly average 13:30 hour net available energy Φ [Φ = (H + λE) (for the tower sites)] for a selection of sites for 2003. The numbers in the x-axis are the month numbers indicating January (as month number 1) to December (as month number 12).

47

**Figure 9.** Comparison of satellite and tower monthly average 13:30 hour **a.** $R_{S\downarrow}$, **b.** $R_{L\downarrow}$ and **c.** $R_{L\uparrow}$ for a selection of sites for which tower data for $R_{S\downarrow}$ (360 data points), $R_{L\downarrow}$ (159 data points) and $R_{L\uparrow}$ (159 data points) were available. The linear fit (solid line) between the two sources of $R_{S\downarrow}$ is, $R_{S\downarrow}(AIRS) = 0.70(\pm0.02)R_{S\downarrow}(tower) + 67.68\ (\pm12.24)$; $r = 0.84\ (\pm0.03)$.The linear fit (solid line) between the two sources of $R_{L\downarrow}$ is, $R_{L\downarrow}(AIRS) = 1.03(\pm0.03)R_{L\downarrow}(tower) - 36.91\ (\pm10.05)$; $r = 0.95\ (\pm0.03)$. The linear fit (solid line) between the two sources of $R_{L\uparrow}$ is, $R_{L\uparrow}(AIRS) = 0\ 91(\pm0.02)R_{L\uparrow}(tower) + 20.43\ (\pm8.77)$; $r = 0.96\ (\pm0.02)$. The dashed lines are 1:1 in all cases.

(+ EBF; x MF; ○ GRA; * CRO; ∇ ENF; ◊ DBF; □ SAV)